Beam Focusing for Near-Field Multi-User Localization

Qianyu Yang , *Graduate Student Member, IEEE*, Anna Guerra, *Member, IEEE*, Francesco Guidi , *Member, IEEE*,
Nir Shlezinger , *Senior Member, IEEE*, Haiyang Zhang , *Member, IEEE*, Davide Dardari , *Fellow, IEEE*,
Baoyun Wang , *Member, IEEE*, and Yonina C. Eldar , *Fellow, IEEE*

Abstract—Extremely large-scale antenna arrays are poised to play a pivotal role in sixth-generation (6G) networks. Utilizing such arrays often results in a near-field spherical wave transmission environment, enabling the generation of focused beams, which introduces new degrees of freedom for wireless localization. In this paper, we consider a beam-focusing design for localizing multiple sources in the radiating near-field. Our formulation accommodates various expected types of implementations of large antenna arrays, including hybrid analog/digital architectures and dynamic metasurface antennas (DMAs). We consider a direct localization estimation method exploiting curvature-of-arrival of impinging spherical wavefront to obtain user positions. In this regard, we adopt a two-stage approach configuring the array to optimize near-field positioning. In the first step, we focus only on adjusting the array coefficients, assuming actual user positions have been known, to minimize the estimation error. We obtain a closed-form approximate solution based on projection and a better one based on the Riemann gradient algorithm. We then extend this approach to localize and focus the beams simultaneously via a sub-optimal iterative approach that does not rely on such pre knowledge of positions. The simulation results show that near-field localization accuracy based on a hybrid array or DMA can achieve performance close to that of fully digital arrays at a lower cost, and DMAs can attain better performance than hybrid solutions with the same aperture.

Index Terms—Near-field multi-user localization, hybrid analog/digital array, dynamic metasurface antennas.

I. INTRODUCTION

IN sixth generation (6G) networks, radio positioning is set to see significant advancements and widespread usage [1], [2], [3], [4]. The deployment of extremely large-scale antenna arrays and the use of high frequencies will greatly enhance radio frequency (RF) positioning accuracy, particularly in scenarios where global positioning system (GPS) signals are inaccessible, such as indoor positioning environments. However, two key challenges and opportunities emerge as dominant factors affecting RF localization. Firstly, combining extremely large-scale antennas and high frequencies often leads to RF signaling occurring within the radiating near-field region. In this region, the commonly used planar wavefront approximation, prevalent in far-field systems, no longer holds [5], [6]. Additionally, implementing arrays with a large number of antenna elements incurs substantial costs when using conventional fully digital designs, where each antenna necessitates a dedicated RF chain [7]. Consequently, extremely large-scale antenna arrays in 6G networks often operate with fewer RF chains than elements and incorporate some degree of analog processing [8].

Source localization can be regarded as estimating two parameters of the users, i.e., their angle and distance with respect to the reference, e.g., a base station. In far-field operating conditions, this typically becomes a joint estimation problem [9], [10]: obtaining the angle estimation from angle of arrival (AOA) and obtaining the distance estimation from time of arrival (TOA) or the received signal strength (RSS) [11], which requires precise synchronization and/or multiple access points participation [12]. In contrast, in the radiating near field, new degrees of freedom arise from the non-negligible spherical shape of the wavefront, which can be exploited to enhance wireless localization, enabling direct localization [13], [14], [15]. Additionally, unlike the TOA-based schemes, there is no need to use a wideband signal in direct localization, i.e., a near-field user can be localized

Qianyu Yang and Baoyun Wang are with the School of Communication and Information Engineering, Nanjing University of Posts and Telecommunications, Nanjing 210049, China (e-mail: 2020010207@njupt.edu.cn; bywang@njupt.edu.cn).

Anna Guerra and Davide Dardari are with the Department of Electrical, Electronic, and Information Engineering "Guglielmo Marconi" - DEI-CNIT, University of Bologna, 47521 Cesena, Italy (e-mail: anna.guerra3@unibo.it; davide.dardari@unibo.it).

Francesco Guidi is with the National Research Council of Italy, IEIIT, 40136 Bologna, Italy (e-mail: francesco.guidi@cnr.it).

Nir Shlezinger is with the School Of Electronics and Communication Engineering, Ben-Gurion University of the Negev, Be'er-Sheva 8410501, Israel (e-mail: nirshl@bgu.ac.il).

Haiyang Zhang is with the School of Communication and Information Engineering, Nanjing University of Posts and Telecommunications, Nanjing 210049, China, and also with the National Mobile Communications Research Laboratory, Southeast University, Nanjing 210096, China (e-mail: haiyang.zhang@njupt.edu.cn).

Yonina C. Eldar is with the Faculty of Math and CS, Weizmann Institute of Science, Rehovot 7610001, Israel (e-mail: yonina.eldar@weizmann.ac.il).

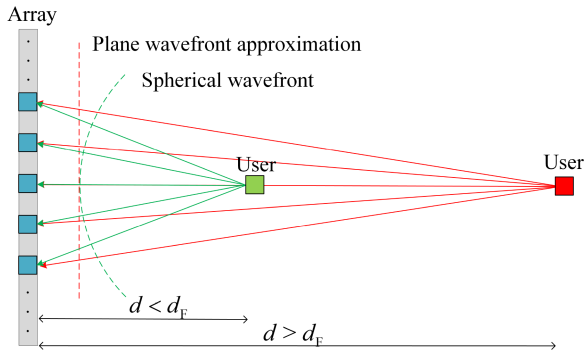Digital Object Identifier 10.1109/TVT.2025.3551502

Fig. 1. Spherical wavefront *vs.* plane wavefront.

using a narrowband signal. This, for instance, is convenient in integrated sensing and communications (ISAC), where fewer radio resources can be dedicated to the sensing part [16].

Specifically, as shown in Fig. 1, when the distance d between the user and the array is less than the Fraunhofer distance d_F, the user is considered to lie in the radiative near-field (Fresnel) region. In such cases, one can directly calculate the user's position, i.e., distance and azimuth, based on the curvature of the spherical wavefront, i.e., one can directly localize in the radiating near-field by estimating the curvature of arrival (COA). On the contrary, when $d > d_F$, the user is in the far-field, and the wavefront of the transmitted signal would be approximated as a plane. In this case, one can only calculate the angle using the approximation of the plane waves and then obtain the distance from the delay information of the incoming signal. The mean squared error (MSE) of this two-step localization algorithm requires calculating the two-step error separately, which typically tends to achieve sub-optimal performance compared to direct localization [17].

COA-based localization was widely used in acoustic or microwave signaling [18], [19], and it has only recently been considered for wireless communications at high-frequency bands [20], [21], [22], [23], [24], [25], [26], [27]. The recent studies of COA-based near-field localization for 6G include the characterization of the Cramér Rao Bound [20], [21]; the investigation of reconfigurable intelligent surface-assisted configurations [22], [23], [24]; the derivations of ad-hoc localization and tracking approaches [25], [27]; the inclusion of hardware impairments into the performance [28]; as well as the near/far hybrid field channel estimation [29]. Several COA-based localization works have focused on MUSIC-based processing and its simplified versions [26], [30], [31]. As an example, in [26], a reduced-dimension MUSIC algorithm for near-field source localization is proposed to avoid the 2D spectral search (i.e., angle and distance), which has been further expanded to 3D application scenarios [31].

Most works on near-field localization consider fully digital antenna architectures, focusing on the enhanced beamforming capability of the near field. However, such antennas are expected to be too costly and power-consuming for realizing large arrays in some 6G settings [32]. The challenges associated with achieving fully connected extremely large-scale arrays operating at high frequencies sparked a growing interest in antenna

architectures operating with reduced RF chains [8]. The electromagnetic lens [33] has the potential to combat the complexity of fully digital architectures and has promoted several studies on its application in near-field localization [17], [34]. However, obtaining flexible and reconfigurable lenses requires complex and costly phase profile control units [17].

An alternative solution for mitigating the complexity of fully digital architectures is to employ hybrid solutions that entail the adoption of conventional antenna technologies (e.g., based on patch arrays) while connecting multiple antennas or panels to an RF chain using dedicated analog circuitry [35]. Such a solution is often implemented using complex gain filter [36], vector modulators [32], phase-shifting networks [37], or switch-based operation [8]. For example, [23] employs the hybrid reconfigurable intelligent surface in near-field user localization and obtains improved performance of localization by optimizing the hybrid reconfigurable intelligent surface configuration. Another emerging technology is based on dynamic metasurface antennas (DMAs), which inherently operates with reduced RF chains without dedicated analog circuitry [38]. DMAs have been shown to support high-rate communications with reduced RF chains in far-field [39] and near-field [40] wireless communication.

However, the application of DMA or hybrid array for localization in radiating near-field has received limited attention in the literature. Near-field single-user location estimation for 6G systems using DMAs has been preliminary studied in [41] for a single-user scenario and was first proposed as a beam focusing model for DMA tuning. On this basis, [42] further analyzed the focus gain loss caused by the mismatch between the DMA focusing position and the actual user position, and design a non-uniform coordinate grid for effectively sampling the user area of interest. Here, we extend the above analysis to the near-field multiple-user case, discussing the near-field localization based on the DMA and, more generally, on hybrid arrays. This extension renders some conclusions previously derived from single-user scenarios no longer applicable due to the bringing of inter-user interference, necessitating the development of a more comprehensive framework for near-field multiple-user localization.

The main contributions are summarized as follows.

- We introduce a COA-based localization method for simultaneously localizing and beam focusing in the radiating near field. We specialize our design to different antenna architectures, including fully digital arrays, hybrid arrays, and DMAs. Notably, the proposed scheme allows for reducing the number of RF chains with respect to common schemes using fully digital antennas. We illustrate how dimensionality reduction of the received signal and inherent analog processing impact the maximum likelihood estimation (MLE) of the user location.
- We propose a two-stage strategy for configuring the array to enhance near-field positioning by formulating the analog processing of DMA and hybrid antenna arrays as a form of precoding for near-field beam focusing [40]. This makes it possible to improve the estimation accuracy of user position by optimizing the adjustable coefficients of DMAs tuning or analog phase-shifter configuration.

- The first stage involves adjusting the array coefficients based on the presumed knowledge of user positions to minimize estimation errors. This approach yields two approximate solutions, one in closed form and another one that achieves better performance entailing the use of the Riemann gradient algorithm.
- Then, we extend our design into a sub-optimal iterative method that does not necessitate such prior knowledge, achieving comparable performance to the optimal method albeit with a slightly higher number of iterations. Notably, in this case, the proposed joint localization and beam-focusing method is based on internal iterations carried out by the receiver, avoiding frequent remote interactions.
- We provide an extensive numerical analysis to demonstrate that the proposed solution can approach the performance achieved with costly fully digital antennas by setting a suitable number of iterations that gradually refine the focused beam generated.

The rest of the paper is organized as follows: Section II describes the considered antenna architectures and corresponding signal models. Then, it introduces the COA-based multi-source localization algorithm and formulates the problem for optimization DMA tuning or hybrid phase-shifter setting. The proposed optimization algorithm is derived in Sections III, while Section IV presents the achieved results. Finally, Section V provides concluding remarks.

Notations: Scalar variables, vectors, and matrices are represented with lower letters, lower bold letters, and capital bold letters, respectively (e.g., x, $\mathbf{x}$, and $\mathbf{X}$, respectively). The term $\mathbb{C}^{N \times N}$ denotes a complex space of dimension $N \times N$, the superscripts $(\cdot)^T$ and $(\cdot)^H$ denote the transpose and Hermitian transpose, respectively, and $|\cdot|$ is the absolute value operator, and $\|\cdot\|$ denotes the Frobenius norm. $\mathbf{1}_m$ denotes a m-dimensional all one vector.

II. SYSTEM MODEL

In this section, we first introduce the considered array architectures in Section II-A, including fully digital arrays, hybrid arrays, and DMAs, and formulate the corresponding received signal model in Section II-B. Then, in Section II-C, we present the COA-based localization method for near-field sources and formulate the optimization problem of designing adjustable coefficients of hybrid arrays and DMAs to improve the accuracy of source position estimation.

A. Array Architecture

We consider three types of antenna architectures, as shown in Fig. 2, that are introduced separately in the following subsections. For convenience, the antennas of the three architectures are placed in a rectangular arrangement with N_d rows and N_e columns, with an overall of $N = N_d N_e$ elements.

a) Fully digital architecture: Fully digital antennas, where processing is carried out only in digital, are widely assumed due to their high flexibility [43]. In such architectures, each element is connected to a dedicated RF chain, as illustrated in Fig. 2(a), and, thus, it results in a costly architecture when large-scale
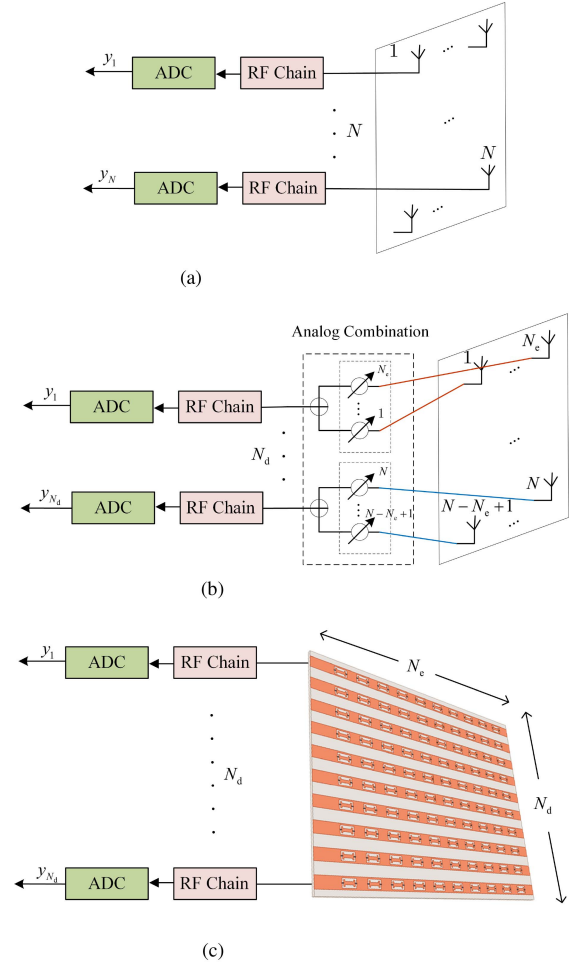

Fig. 2. Considered array architectures. (a) Fully digital architecture. (b) Hybrid architecture. (c) DMA architecture.

arrays are employed. In this paper, the fully digital array represents the baseline architecture to measure how much analog pre-processing (stemming from RF chain reduction) affects the localization performance.

b) Hybrid architecture: A candidate technology to reduce the number of RF chains is represented by hybrid antenna arrays (e.g., based on patch arrays), where a large number of antennas is connected to a smaller number of RF chains using dedicated analog circuitry, such as phase-shifting networks [44]. Phase-shifter-based hybrid arrays combine digital signal processing with some constrained level of analog signal processing. As shown in Fig. 2(b), for the hybrid array, each antenna is connected to an RF chain through an independent phase-shifter, and an analog combination for antenna outputs reduces the number of RF chains. Specifically, the array is divided as N_d line sub-arrays composed of N_e elements arranged uniformly, and each line sub-array is operated by a fully connected phase-shifter network with a single RF chain. Therefore, the signal captured at the ith RF chain is given by

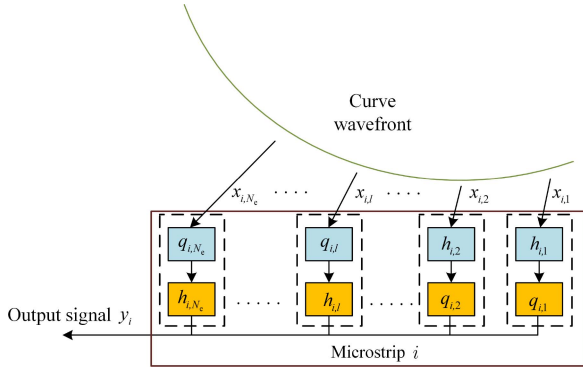$$y_{\mathrm{h}i} = \sum_{l=1}^{N_e} q_{i,l} x_{i,l}, \tag{1}$$

Fig. 3. Signal reception at the i-th microstrip.

where $x_{i,l}$ is the received signal from the corresponding element. Here $q_{i,l}$ denotes the phase of phase-shifter, which satisfies

$$q_{i,l} \in \mathcal{F} \triangleq \left\{ e^{j\phi_{i,l}} \mid \phi_{i,l} \in [0, 2\pi] \right\}, \forall i, l. \tag{2}$$

c) DMA: DMA is an emerging antenna technology that inherently implements RF chain reduction with low cost and power consumption and reconfigurable analog processing, using radiating metamaterial elements embedded onto the surface of a waveguide [40]. As shown in Fig. 2(c), the DMA architecture comprises multiple waveguides (termed microstrips), each containing multiple metamaterial elements. The received signals of each element within each microstrip are aggregated into a corresponding RF chain [38]. Since the frequency response of each element can be individually adjusted [45], the number of RF chains to be processed translates from the number of receiving elements to the number of microstrips. The elements in each microstrip are usually sub-wavelength-spaced, meaning more elements can be packed in a given aperture compared to the conventional architectures.

Fig. 3 depicts signal reception via a microstrip with multiple elements: The signals impinging on the DMA elements propagate inside the waveguide and are captured at the output port. The output of each microstrip is thus modeled as a weighted sum of these received signals; we consider the case where the response of the elements is frequency flat and focus on the Lorentzian-constrained phase model of the metamaterial elements frequency response [46]. Hence, the signal captured at the output of the ith microstrip, after undergoing the elements' response and propagating inside the waveguide, is given by:

$$y_i = \sum_{l=1}^{N_e} h_{i,l} \, q_{i,l} \, x_{i,l}, \tag{3}$$

where $h_{i,l}$ encapsulates the effect of signal propagation inside the microstrip, given by [39]

$$h_{i,l} = e^{-\rho_{i,l}(\alpha_i + j\beta_i)}, \tag{4}$$

where α_i is the waveguide attenuation coefficient, β_i is the wavenumber, and $\rho_{i,l}$ denotes the distance of the l-th element from the output port of the i-th microstrip. Then, the term $q_{i,l}$ denotes the tunable response of the corresponding antenna, and

its feasible settings satisfy the Lorentzian form

$$q_{i,l} \in \mathcal{Q} \triangleq \left\{ \frac{j + e^{j\phi_{i,l}}}{2} \mid \phi_{i,l} \in [0, 2\pi] \right\}, \quad \forall i, l. \tag{5}$$

Comparing (1) and (3), the received signals of both arrays are the result of accumulation, with the difference being that the weighting coefficients are the phase of phase-shifter in the hybrid array and DMA coefficient in DMA, respectively, which follows different constraints as (2) and (5).

B. Received Signal Model

We consider a multi-user localization scenario in which a multi-antenna base station receives pilot signals from M users and estimates their locations. We focus on settings where the number of users is known. In practice, such information can often be reliably estimated from the impinging signals, e.g., [47]. The base station is equipped with one of the three arrays of Fig. 2, i.e., the common fully digital array, the hybrid array, and the DMA. The array aperture and the signaling frequency are assumed to be such that the transmitting user resides in the radiating near-field, i.e., in the Fresnel region (which can be in distances of the order of tens and even hundreds of meters in some 6G settings [6]). Since the user is within the Fresnel region of the base station array, the transmitted signal exhibits a spherical wavefront.

We suppose that all users share the same pilot frequency, and the unified narrowband pilot signal at frequency f_p is emitted by each source with power normalized to one. Thus, the signal received by the l-th antenna of the i-th line array/microstrip at a generic discrete time instance is given by

$$x_{i,l} = \sum_{m=1}^{M} x_{m,i,l} + z_{i,l}. \tag{6}$$

In (6), $z_{i,l}$ is an additive Gaussian noise on the responding antenna with variance σ^2, $x_{m,i,l}$ is the received signal from the m-th user at the corresponding antenna. The latter can be expressed as

$$x_{m,i,l} = \text{g}_{m,i,l} \, c_m, \tag{7}$$

where c_m is the source pilot signal symbol stream satisfies $|c_m|^2 = 1$, $\text{g}_{m,i,l} = a_m e^{-jv_{m,i,l}}$ represents the channel component, with a_m and $v_{m,i,l}$ denoting the channel gain coefficient and the phase due to the distance traveled by the signal, respectively. The gain is expressed as $a_m = \frac{c}{4\pi f_\text{p} d_m}$ with d_m denotes the distance between the array and the source, and the phase is given by

$$v_{m,i,l} \triangleq 2\pi f_\text{p} \frac{d_{m,i,l}}{c}, \tag{8}$$

where $d_{m,i,l}$ is the distance between the corresponding antenna and the source, and c is the speed of light.

Define the vector $\mathbf{x} = [x_{1,1}, \dots, x_{i,l}, \dots, x_{N_\text{d}, N_\text{e}}]^T \in \mathbb{C}^N$. Now, (6) can be written as

$$\mathbf{x} = \sum_{m=1}^{M} \mathbf{g}_m c_m + \mathbf{z} = \mathbf{G} \, \mathbf{c} + \mathbf{z}, \tag{9}$$

where $\mathbf{g}_m = [g_{m,1,1}, \ldots, g_{m,i,l}, \ldots, g_{m,N_d,N_e}]^T \in \mathbb{C}^{N \times 1}$ and $\mathbf{z} = [z_{1,1}, \ldots, z_{i,l}, \ldots, z_{N_d,N_e}]^T \in \mathbb{C}^{N \times 1}$ denote the channel vector and noise vector, respectively. The matrix $\mathbf{G} = [\mathbf{g}_1, \ldots, \mathbf{g}_M] \in \mathbb{C}^{N \times M}$ is the channel matrix, $\mathbf{c} = [c_1, \ldots, c_M]^T$. Since the fully digital array assigned RF chains to all antennas, (9) can also regarded as the output of the fully digital array.

For the hybrid array, by (10), the output vector $\mathbf{y}_h = [y_{h1}, \ldots, y_{hN_d}]^T \in \mathbb{C}^{N_d}$ is given by

$$\mathbf{y}_h = \mathbf{Q}\,\mathbf{x}, \tag{10}$$

where the matrix $\mathbf{Q} \in \mathbb{C}^{N_d \times N}$ represents analog precoding of the hybrid array that satisfies

$$\mathbf{Q}_{n,(i-1)N_e+l} = \begin{cases} q_{i,l} \in \mathcal{F} & i = n, \\ 0 & i \neq n. \end{cases} \tag{11}$$

Similarly, the output of DMA in vector form is given by

$$\mathbf{y}_q = \mathbf{Q}\,\mathbf{H}\,\mathbf{x}, \tag{12}$$

where $\mathbf{H}$ is a $N \times N$ diagonal matrix with diagonal elements $\mathbf{H}_{((i-1)N_e+l,(i-1)N_e+l)} = h_{i,l}$. The matrix $\mathbf{Q} \in \mathbb{C}^{N_d \times N}$ in DMA case denotes the reconfigurable weights of the DMAs. Since we focus on narrowband signaling, for which the elements can be approximated with the Lorentzian-constrained form [40], $\mathbf{Q}$ obeys the following structure:

$$\mathbf{Q}_{n,(i-1)N_e+l} = \begin{cases} q_{i,l} \in \mathcal{Q} & i = n, \\ 0 & i \neq n. \end{cases} \tag{13}$$

We use the same symbol $\mathbf{Q}$ to define the adjustable coefficient matrix in (10) and (12). This is because, as noted above, DMAs and hybrid arrays perform similar operations in the analog domain (with different constraints) and yield similar output forms Accordingly, in the following, we will also generically refer to $\mathbf{y}_h$ and $\mathbf{y}_q$ as $\mathbf{y}$.

C. Problem Formulation

We consider the task of estimating the user positions based on the above output formulas while tuning $\mathbf{Q}$ to achieve an accurate estimate. The fact that the communication takes place in the radiating near-field can be exploited to facilitate localization based on the COA of the impinging signal at different elements. In our preliminary work [41], we delved into single-user near-field localization scenarios where both the array and the user were situated on the same plane. However, in the context of this paper, the single-user approach proves ineffective due to substantial inter-user interference arising from the shared pilot frequency utilized by multiple users. In this paper, we consider the more general localization scenario as illustrated in Fig. 4, with multiple users, all three architectures detailed above, and where the square array is located on different planes with users.

Specifically, we set a reference point (i.e., antenna) located in $(0,0,0)$ for the receiving array, and the square array is standing on the YZ plane, the m-th user is located in (x_m, y_m, z_m), at distance d_m, according to an azimuth θ_m and elevation angle γ_m with respect to the source (see Fig. 4), respectively.
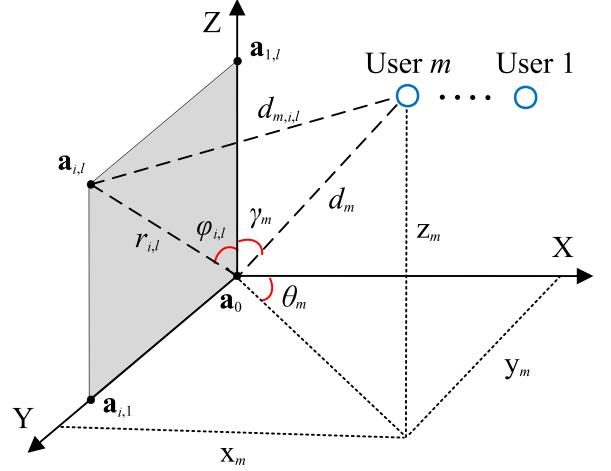

Fig. 4. Relative position relationships between source and array. The $\mathbf{a}_0$ is reference antenna, whereas the antenna of the i-line and l-row is at $\mathbf{a}_{i,l}$.

Further, the l-th antenna of the i-th row of the array is located at $(0, y_{i,l}, z_{i,l})$, with polar coordinate expressed as $(r_{i,l}, \varphi_{i,l})$. The specific geometric relationships between coordinates and reference positions are as follows

$$x_m = d_m \sin\gamma_m \cos\theta_m,$$
$$y_m = d_m \sin\gamma_m \sin\theta_m,$$
$$z_m = d_m \cos\gamma_m. \tag{14}$$

According to the triangular relationship between reference points, the antenna, and the user, $d_{m,i,l}(d_m, \theta_m, \gamma_m)$ can be expressed as [25]:

$$d_{m,i,l}(d_m, \theta_m, \gamma_m) = \sqrt{r_{i,l}^2 + d_m^2 - 2r_{i,l}d_m g(\theta_m, \gamma_m)}, \tag{15}$$

where $g(\theta_m, \gamma_m)$ is a geometric term given by

$$g(\theta_m, \gamma_m) = \sin\varphi_{i,l}\sin\theta_m\sin\gamma_m + \cos\varphi_{i,l}\cos\gamma_m. \tag{16}$$

The operation in the radiating near-field implies that none of the terms in (15) can be neglected. Thus, (15) determines the relationship between the user location and the phase profile, which is highly nonlinear and is retained at the above output. Moreover, common multi-user localization methods (e.g., signal subspace techniques) are inapplicable due to the shared pilot signal. Therefore, a possible solution for estimating the user position is to compute the MLE given by

$$\left(\hat{d}_\mathcal{M}, \hat{\theta}_\mathcal{M}, \hat{\gamma}_\mathcal{M}\right) = \arg\max_{\mathbf{p}_\mathcal{M}} \log p\left(\mathbf{y}; \mathbf{p}_\mathcal{M}\right), \tag{17}$$

where $\log p(\mathbf{y}; \mathbf{p}_\mathcal{M})$ is the log-likelihood function of $\mathbf{y}$. Here $\mathbf{p}_\mathcal{M}$ and $(\hat{d}_\mathcal{M}, \hat{\theta}_\mathcal{M}, \hat{\gamma}_\mathcal{M})$ refer to the possible and the estimated user positions set in polar coordinates, respectively, with $\mathbf{p}_\mathcal{M} = (d_\mathcal{M}^\star, \theta_\mathcal{M}^\star, \gamma_\mathcal{M}^\star)$ and $\mathcal{M} = \{1, \ldots, M\}$. For convenience, define $\mathbf{p}_m = (d_m^\star, \theta_m^\star, \gamma_m^\star)$ as the possible position of m-th user, i.e., $\mathbf{p}_\mathcal{M}$ can also expressed as $\mathbf{p}_\mathcal{M} = \{\mathbf{p}_m\}_{m=1}^M$.

Since the received signals of both the hybrid array and the DMA also depend on the adjustable coefficient matrix $\mathbf{Q}$, it results that $\mathbf{Q}$ affects the accuracy of the MLE. Therefore, it

is necessary to design the phase shifters or DMA tuning to facilitate localization for the hybrid array and DMA cases. Due to the similar receive mode, we will discuss DMA-based MLE in the next section and show how our approach extends to hybrid arrays.

III. JOINT LOCALIZATION AND BEAMFOCUSING

In this section, we explore simultaneous multi-user localization and beam focusing using large antenna architectures. As previously mentioned, we concentrate on DMAs, where beam focusing involves tuning its reconfigurable elements. We commence by formulating an alternating projection algorithm for near-field localization for a given DMA configuration in Section III-A. Then, we derive joint localization and beam focusing in two stages. First, we assume that one has prior knowledge of the users' location and develop two DMA tuning schemes in Section III-B, with the former having low complexity and the latter having higher performance. Then, in Section III-C, we extend these designs to also carry out localization, i.e., the actual case that prior knowledge of user location does not exist. This is achieved via an iterative algorithm for joint optimization position estimation and DMA tuning. Finally, in Section III-D, we show that while our method is formulated for DMAs, it can also be naturally adapted to both hybrid phase-shifter-based architectures as well as fully digital ones after some simplification.

A. Localization for Fixed DMA Tuning

We start by considering the case in which the DMA configuration, namely the matrix $\mathbf{Q}$, is fixed. For such setups, we propose a method for localizing the users.

Assuming N_{T} samples are collected for MLE during each observation time window, the t-th sample is marked as $\mathbf{y}(t)$, $t = 1, \ldots, N_{\mathrm{T}}$. According to (12), once we obtain a sufficient number of receiving samples, the log-likelihood function of $\mathbf{y}$ can be expressed as

$$\log p\left(\mathbf{y}; \mathbf{p}_{\mathcal{M}}\right) \propto \sum_{t=1}^{N_{\mathrm{T}}} \|\mathcal{P}\left[\mathbf{S}\left(\mathbf{p}_{\mathcal{M}}, \mathbf{Q}\right)\right] \mathbf{y}(t)\|^2, \quad (18)$$

where $\mathcal{P}$ denotes the projection operator, which, when applied to a matrix $\mathbf{X}$, is given by

$$\mathcal{P}\left[\mathbf{X}\right] = \mathbf{X}\left[\mathbf{X}^H \mathbf{X}\right]^{-1} \mathbf{X}^H.$$

Projection in (18) is applied to $\mathbf{S}(\mathbf{p}_{\mathcal{M}}, \mathbf{Q}) = \mathbf{Q}\mathbf{H}\mathbf{S}_{\mathrm{a}}(\mathbf{p}_{\mathcal{M}})$, with $\mathbf{S}_{\mathrm{a}}(\mathbf{p}_{\mathcal{M}}) = [\mathbf{s}_1, \ldots, \mathbf{s}_M] \in \mathbb{C}^{N \times M}$ denoting the steering matrix of the array[1] where each steering vector is given by

$$\mathbf{s}_m = \left[\mathrm{a}_m e^{-j v_{1,1}(\mathbf{p}_m)}, \ldots, \mathrm{a}_m e^{-j v_{m, N_{\mathrm{d}}, N_{\mathrm{e}}}(\mathbf{p}_m)} \right]^T, \quad (19)$$

where $v_{m,i,l}(\mathbf{p}_m)$ is obtained from (8) and (15). Note that $\mathbf{s}_m = \mathbf{g}_m$ only if $\mathbf{p}_m = (d_m, \theta_m, \gamma_m), \forall m \in \mathcal{M}$.

The maximization of the (18) is a nonlinear, multi-dimensional maximization problem, and thus, direct processing

would yield a significant amount of complexity. The alternating projection (AP) maximization technique is a conceptually simple technique for multi-dimensional maximization. The technique converts the multi-dimensional maximization problem into multiple one-dimensional problems by alternating iterations. Specifically, the projection operator $\mathcal{P}[\mathbf{S}(\mathbf{p}_{\mathcal{M}}, \mathbf{Q})]$ can be rewritten as [48]

$$\mathcal{P}\left[\mathbf{S}\left(\mathbf{p}_{\mathcal{M}}, \mathbf{Q}\right)\right] = \mathcal{P}\left[\mathbf{S}\left(\mathbf{p}_{\mathcal{M}-m}, \mathbf{Q}\right)\right] + \mathcal{P}\left[\overline{\mathbf{S}}\left(\mathbf{p}_m, \mathbf{Q}\right)\right], \quad (20)$$

where $\mathbf{S}(\mathbf{p}_{\mathcal{M}-m}, \mathbf{Q}) \in \mathbb{C}^{N_{\mathrm{d}} \times M-1}$ is the steering matrix based on $\mathbf{p}_{\mathcal{M}-m}$, while $\mathbf{p}_{\mathcal{M}-m}$ is the difference set of $\mathbf{p}_{\mathcal{M}}$ with $\mathbf{p}_m$, i.e., $\mathbf{p}_{\mathcal{M}-m} = \{\mathbf{p}_t\}_{t=1, t \neq m}^M$. In (20), $\overline{\mathbf{S}}(\mathbf{p}_m, \mathbf{Q}) \in \mathbb{C}^{N_{\mathrm{d}} \times 1}$ denotes the residual of $\mathbf{Q}\mathbf{H}\mathbf{s}_m$ when projected on $\mathbf{S}(\mathbf{p}_{\mathcal{M}-m}, \mathbf{Q})$, which is given by

$$\overline{\mathbf{S}}\left(\mathbf{p}_m, \mathbf{Q}\right) = \left(\mathbf{I}_{N_{\mathrm{d}}} - \mathcal{P}\left[\mathbf{S}\left(\mathbf{p}_{\mathcal{M}-m}, \mathbf{Q}\right)\right]\right) \mathbf{Q}\mathbf{H}\mathbf{s}_m. \quad (21)$$

From (20), for a given $\mathbf{Q}$, once $\mathbf{p}_{\mathcal{M}-m}$ has been fixed, $\mathcal{P}[\mathbf{S}(\mathbf{p}_{\mathcal{M}}, \mathbf{Q})]$ would only be determined by $\mathbf{p}_m$, and thus the first term of (20) can be ignored. Consequently, the maximization of the (18) can be iterative, at every iteration a maximization is performed with respect to a single parameter while all the other parameters are held fixed.

Therefore, by substituting (20) into (18), the problem (17) can be simplified as solving M sub-problem, and the m-th sub-problem is expressed as

$$\log p\left(\mathbf{y}; \mathbf{p}_m\right) \propto \sum_{t=1}^{N_T} \|\mathcal{P}\left[\overline{\mathbf{S}}\left(\mathbf{p}_m, \mathbf{Q}\right)\right] \mathbf{y}(t)\|^2. \quad (22)$$

Based on this formulation, one can compute (22) and iteratively localize the user by AP method when $\mathbf{Q}$ is fixed, the detailed process is summarized as Algorithm 1. Notably, such an algorithm contains an initial position estimation because precise initialization is crucial as it can greatly enhance the overall convergence speed of the iteration process. This initial estimation starts from a single-user scenario to estimate the first user, then fixes existing estimates and continuously increases users until obtaining the last estimate.

The computation of Algorithm 1 requires a given $\mathbf{Q}$. Therefore, the fact that the accuracy of this estimate depends on $\mathbf{Q}$ allows us to use the above MLE as guidelines for tuning the DMA along with the localization task.

B. DMA Tuning for Given Positions

The formulation of the localization log-likelihood in the previous sections serves as a starting point for deriving our joint localization and beamfocusing method. We do this in two stages. First, we consider designing the DMA tuning to optimize the MLE in (17), i.e., ignoring, for now, the fact that its computation requires knowledge of the users' positions.

For ease of analysis, as in [18], we rewrite (18) as

$$\log p\left(\mathbf{y}; \mathbf{p}_{\mathcal{M}}\right) \propto \operatorname{tr}\left[\mathcal{P}\left[\mathbf{S}\left(\mathbf{p}_{\mathcal{M}}, \mathbf{Q}\right)\right] \mathbf{R}\right], \quad (23)$$

where $\mathbf{R}$ is the empirical average of $\mathbf{y}\mathbf{y}^H$ over the observed time window, which can be approximated to the statistical covariance, which expressed as expressed as $\mathbf{R} =$

---

[1] In the near field, the steering matrix/vector concept loses its usual meaning as it cannot be identified as a unique steering direction. Despite that, in this paper, we still adopt this term in a wide sense.

Algorithm 1: AP-Based Localization with Fixed DMA Tuning.

Input: M; $\mathbf{Q}$; $\{\mathbf{y}(t)\}_{t=1}^{N_T}$; The maximal iteration number K.
Initialize: Set $k = 1$; The initial position set $\mathbf{p}_{\mathcal{M}} = \{\emptyset\}$;
  The projection operation $\mathcal{P}[\mathbf{S}(\mathbf{p}_{\mathcal{M}}, \mathbf{Q})] = \mathbf{0}$.
For $m = 1 : M$
  1: Obtain $\mathbf{p}_m^0 = \mathbf{p}_m$ by searching for $\mathbf{p}_m$ that maximize
  (22), where $\overline{\mathbf{S}}(\mathbf{p}_m, \mathbf{Q})$ is calculated by

  $$\overline{\mathbf{S}}(\mathbf{p}_m, \mathbf{Q}) = (\mathbf{I}_{N_d} - \mathcal{P}[\mathbf{S}(\mathbf{p}_{\mathcal{M}}, \mathbf{Q})])\mathbf{Q}\mathbf{H}\mathbf{s}_m$$

  2: Update the position set as $\mathbf{p}_{\mathcal{M}} = \mathbf{p}_{\mathcal{M}} \cup \mathbf{p}_m^0$.
  3: Update the projection operation as

  $$\mathcal{P}[\mathbf{S}(\mathbf{p}_{\mathcal{M}}, \mathbf{Q})] = \mathcal{P}[\mathbf{S}(\mathbf{p}_{\mathcal{M}}, \mathbf{Q})] + \mathcal{P}[\overline{\mathbf{S}}(\mathbf{p}_m^0, \mathbf{Q})]$$

End
  4: Obtain the initiation position set $\mathbf{p}_{\mathcal{M}} = \{\mathbf{p}_m^0\}_{m=1}^M$.
While $k \leq K$ **do**
  For $m = 1 : M$
  5: Obtain $\mathbf{p}_m^k = \mathbf{p}_m$ by searching for $\mathbf{p}_m$ that maximize
  (22), where $\overline{\mathbf{S}}(\mathbf{p}_m, \mathbf{Q})$ is obtained by calculating (21).
  6: Update position set as $\mathbf{p}_{\mathcal{M}} = \mathbf{p}_{\mathcal{M}-m} \cup \mathbf{p}_m^k$.
  7: Update $\mathcal{P}[\mathbf{S}(\mathbf{p}_{\mathcal{M}}, \mathbf{Q})]$ with $\overline{\mathbf{S}}(\mathbf{p}_m^k, \mathbf{Q})$ through (20).
  End
  8: $k = k + 1$.
End while
Output: The position estimation $\mathbf{p}_{\mathcal{M}} = \{\mathbf{p}_m^K\}_{m=1}^M$.

$\mathbf{Q}\mathbf{H}(\mathbf{G}\mathbf{G}^H + \sigma^2\mathbf{I}_N)\mathbf{H}^H\mathbf{Q}^H$. For convenience, we define a function $f(\mathbf{p}_{\mathcal{M}}, \mathbf{Q})$ as:

$$f(\mathbf{p}_{\mathcal{M}}, \mathbf{Q}) = \text{tr}[\mathcal{P}[\mathbf{S}(\mathbf{p}_{\mathcal{M}}, \mathbf{Q})]\mathbf{R}]. \tag{24}$$

The MLE computation can be regarded as a search process over distance and angle to maximize (24), and the maximum value of (24) is expected to converge to the true user position, i.e., $(\hat{d}_{\mathcal{M}}, \hat{\theta}_{\mathcal{M}}, \hat{\gamma}_{\mathcal{M}}) = (d_{\mathcal{M}}, \theta_{\mathcal{M}}, \gamma_{\mathcal{M}})$. Therefore, we aim to design $\mathbf{Q}$ to maximize (24) at the actual position, i.e., set $\mathbf{p}_{\mathcal{M}}^* = (d_{\mathcal{M}}, \theta_{\mathcal{M}}, \gamma_{\mathcal{M}})$, and considering the following problem:

$$\max_{\mathbf{Q}} f(\mathbf{p}_{\mathcal{M}}^*, \mathbf{Q})$$

$$\text{s.t. } (5), (13). \tag{25}$$

Problem (25) is non-convex because of the Lorentzian-constrained $\mathcal{Q}$ form in (5). To overcome this limitation, we introduce below two approximate solutions to relax the problem (25) into the solvable convex problem to obtain an approximate solution.

1) Approximate Solution Based on Projection: Substituting the definition of $\mathbf{R}$ into problem (25), and using $\mathbf{P}_{\mathbf{S}_D(\mathbf{p}_{\mathcal{M}}^*, \mathbf{Q})}\mathbf{Q}\mathbf{H}\mathbf{G}\mathbf{G}^H\mathbf{H}^H\mathbf{Q}^H = \mathbf{Q}\mathbf{H}\mathbf{G}\mathbf{G}^H\mathbf{H}^H\mathbf{Q}^H$, the problem (25) can be explicitly rewritten to

$$\max_{\mathbf{Q}} \text{tr}[\mathbf{Q}\mathbf{H}\mathbf{G}\mathbf{G}^H\mathbf{H}^H\mathbf{Q}^H]$$

$$+ \text{tr}[\mathcal{P}[\mathbf{S}(\mathbf{p}_{\mathcal{M}}, \mathbf{Q})]\sigma^2\mathbf{Q}\mathbf{H}\mathbf{H}^H\mathbf{Q}^H]$$

$$\text{s.t. } (5), (13). \tag{26}$$

The Lorentzian-constrained $\mathcal{Q}$ form in (5) makes the problem (26) still difficult to solve. Following [40], we tackle this by relaxing the Lorentzian constraint to the phase-only weights constraint with constant amplitude and arbitrary phase, i.e. (2), the problem can be regarded as

$$\max_{\mathbf{Q}} \text{tr}[\mathbf{Q}\mathbf{H}\mathbf{G}\mathbf{G}^H\mathbf{H}^H\mathbf{Q}^H]$$

$$\text{s.t. } \mathbf{Q}_{n,(i-1)N_e+l} = \begin{cases} q_{i,l} \in \mathcal{F} & i = n. \\ 0 & i \neq n. \end{cases} \tag{27}$$

The second factor of problem (26) is omitted in (27) as it is a constant. This is because following the phase-only weights constraint, we have $\mathbf{Q}\mathbf{H}\mathbf{H}^H\mathbf{Q}^H = \sum_{l=1}^{l=N_e} h_{i,l}^2\mathbf{I}_{N_d}$ and $\text{tr}[\mathcal{P}[\mathbf{S}(\mathbf{p}_{\mathcal{M}}, \mathbf{Q})]] = 1$. Following the definition of $\mathbf{G}$, problem (27) can be rewritten as

$$\max_{\mathbf{Q}} \sum_{m=1}^M \text{tr}[\mathbf{Q}\mathbf{H}\mathbf{g}_m\mathbf{g}_m^H\mathbf{H}^H\mathbf{Q}^H]$$

$$\text{s.t. } \mathbf{Q}_{n,(i-1)N_e+l} = \begin{cases} q_{i,l} \in \mathcal{F} & i = n. \\ 0 & i \neq n. \end{cases} \tag{28}$$

Since $M > 1$, the DMA tunable coefficients, i.e., $q_{i,l}$, would not be enough to perfectly adjust for the phase of the arrived signals. But inspired by the phase design of RIS in [22], we divide (28) into multiple sub-problems. Consequently, the optimal solution to (28) can be regarded as finding a trade-off between the solutions of these sub-problems. The solution to (28) is stated in the following theorem.

Theorem 1: The solution to (28), represented as $\mathbf{Q}^*$, can be obtained by setting each non-zero element to $q_{i,l}^* = e^{j\psi_{i,l}^*}$, with $\psi_{i,l}^* = \frac{\sum_{m=1}^M v_{m,i,l}}{M} + \rho_{i,l}\beta_i$.

Proof: The proof is given in Appendix A. ∎

As $q_{i,l}^*$ in Theorem 1 does not satisfy the Lorentzian form, we project it onto (5) following [40]. The resulting weight is $\hat{q}_{i,l} = \frac{j + e^{j\psi_{i,l}^*}}{2}$, and though it is not the optimal solution of (26), it provides a simple closed form solution but that guarantees reliable positioning performance as shown in the numerical results.

In the following, we propose an alternative approach where we transform the Lorentz constraint into a phase-only constraint and use the Riemannian conjugate gradient algorithm to obtain the solution.

2) Approximate Solution Based on the Riemannian Conjugate Gradient Algorithm: In fact, the first factor of the objective function in (26) represents the effect of DMA tuning on the received signals, while the second factor represents the effect of DMA tuning on noise. However, the localization information we are interested in is only encapsulated in the received signals. By omitting the second factor of the objective function in (26), we obtain the following problem:

$$\max_{\mathbf{Q}} \text{tr}[\mathbf{Q}\mathbf{H}\mathbf{G}\mathbf{G}^H\mathbf{H}^H\mathbf{Q}^H]$$

$$\text{s.t. } \mathbf{Q}_{n,(i-1)N_e+l} = \begin{cases} q_{i,l} \in \mathcal{Q} & i = n. \\ 0 & i \neq n. \end{cases} \tag{29}$$

Then we introduce following inequality:

$$
\operatorname{tr}\left[\mathcal{P}\left[\mathbf{S}\left(\mathbf{p}_{\mathcal{M}}, \mathbf{Q}\right)\right] \sigma^{2} \mathbf{Q} \mathbf{H} \mathbf{H}^{H} \mathbf{Q}^{H}\right] \operatorname{tr}\left[\mathbf{G} \mathbf{G}^{H}\right]
$$
$$
\geq \operatorname{tr}\left[\mathbf{H}^{H} \mathbf{Q}^{H} \mathcal{P}\left[\mathbf{S}\left(\mathbf{p}_{\mathcal{M}}, \mathbf{Q}\right)\right] \sigma^{2} \mathbf{Q} \mathbf{H} \mathbf{G} \mathbf{G}^{H}\right]
$$
$$
= \sigma^{2} \operatorname{tr}\left[\mathbf{Q} \mathbf{H} \mathbf{G} \mathbf{G}^{H} \mathbf{H}^{H} \mathbf{Q}^{H}\right], \tag{30}
$$

the inequality in (30) use a matrix trace inequality: For any semidefinite matrix, e.g, $\mathbf{A} \succeq \mathbf{0}$ and $\mathbf{B} \succeq \mathbf{0}$, we have

$$
\operatorname{tr}\left[\mathbf{A}\right] \operatorname{tr}\left[\mathbf{B}\right] \geq \operatorname{tr}\left[\mathbf{A}\mathbf{B}\right], \tag{31}
$$

As $\operatorname{tr}[\mathbf{G}\mathbf{G}^{H}] = MN$, by substituting (30) into (26), the optimization of (29) can be regarded as maximizing the lower bound of the objective function of (26). Therefore, we can relax (26) as solving (29). Likewise (27), (29) can be rewritten as

$$
\max_{\mathbf{Q}} \sum_{m=1}^{M} \operatorname{tr}\left[\mathbf{Q} \mathbf{H} \mathbf{g}_{m} \mathbf{g}_{m}^{H} \mathbf{H}^{H} \mathbf{Q}^{H}\right]
$$
$$
\text{s.t. } \mathbf{Q}_{n,(i-1)N_{\mathrm{e}}+l} = \begin{cases} q_{i,l} \in \mathcal{Q} & i = n. \\ 0 & i \neq n. \end{cases} \tag{32}
$$

With the Lorentzian constraint, (32) would not obtain a closed-form solution following Theorem 1. To proceed, we define the vector $\mathbf{q} = vec(\mathbf{Q}) \in \mathbb{C}^{N_d N \times 1}$, and thus we have $\mathbf{Q}\mathbf{H}\mathbf{g}_m = (\mathbf{H}\mathbf{g}_m)^T \otimes \mathbf{I}_{N_d}\mathbf{q}$, define $\mathbf{W} = (\mathbf{H}\mathbf{g}_m)^T \otimes \mathbf{I}_{N_d}$, (32) can further rewritten as

$$
\max_{\mathbf{q}} \sum_{m=1}^{M} \mathbf{q}^{H} \mathbf{W}^{H} \mathbf{W} \mathbf{q}
$$
$$
\text{s.t. } \mathbf{q}_{n+((i-1)N_{\mathrm{e}}+l-1)N_{\mathrm{d}}} = \begin{cases} q_{i,l} \in \mathcal{Q} & i = n. \\ 0 & i \neq n. \end{cases} \tag{33}
$$

It is easy to verify that the zero elements of $\mathbf{q}$ do not affect the objective function of (33). Hence, (33) can be simplified as

$$
\max_{\overline{\mathbf{q}}} \sum_{m=1}^{M} \overline{\mathbf{q}}^{H} \overline{\mathbf{W}}^{H} \overline{\mathbf{W}} \overline{\mathbf{q}},
$$
$$
\text{s.t. } \overline{q}_{r} \in \mathcal{Q}, \forall r \in \mathcal{A}_{q}, \tag{34}
$$

where $\mathcal{A}_q$ denotes the set of all non-zero elements of $\mathbf{q}$, $\overline{\mathbf{q}} \in \mathbb{C}^{N \times 1}$ is the modified version of $\overline{\mathbf{q}}$ obtained by removing all the zero elements of $\mathbf{q}$, and $\overline{\mathbf{W}}$ is the modified version of $\mathbf{W}$ obtained by removing the elements having the same index as the zero elements of $\mathbf{q}$.

Inspired by [49], to remove the Lorentzian constraint in (34), we define a new vector $\mathbf{b} \in \mathbb{C}^{N \times 1}$ whose r-th element is given by

$$
b_{r} = 2\overline{q}_{r} - e^{j2\pi}, \forall r \in \mathcal{A}_{q}. \tag{35}
$$

By its definition, $\mathbf{b}$ satisfies the phase-only constrained constant modulus, i.e., $b_r \in \mathcal{F} \triangleq \{e^{j\phi_r} \mid \phi_r \in [0, 2\pi]\}$. Meanwhile, according to (35), we have $\overline{\mathbf{q}} = \frac{1}{2}(\mathbf{b} + e^{j2\pi}\mathbf{1}_N)$. Based on these,

(34) can be equivalently written as

$$
\max_{\mathbf{b}} \sum_{m=1}^{M} \frac{1}{4}\left(\mathbf{b} + e^{j2\pi}\mathbf{1}_N\right)^{H} \overline{\mathbf{W}}^{H} \overline{\mathbf{W}} \left(\mathbf{b} + e^{j2\pi}\mathbf{1}_N\right),
$$
$$
\text{s.t. } b_{r} \in \mathcal{F}, \forall r \in \mathcal{A}_{q}. \tag{36}
$$

The search space in (36) is a product of N complex circles, a Riemannian submanifold of $\mathbb{C}^N$. Therefore, (36) can be tackled using the Riemannian conjugate gradient (RCG) algorithm. Defining the objection function of (36) as $g(\mathbf{b})$, the solution of (36) is thus iteratively updated based on the following formula:

$$
\mathbf{b}^{(t+1)} = \mathcal{R}_t\left(\mathbf{b}^{(t)} + \boldsymbol{\epsilon}^{(t)} \boldsymbol{\eta}^{(t)}\right), \tag{37}
$$

where $\mathbf{b}^{(t+1)}$ is the updated point from the current point $\mathbf{b}^{(t)}$ and t is the iteration number, the initial $\mathbf{b}^{(0)}$ could be obtained by the solution of the projection method above. Thus the RCG-based solution can be regarded as an improvement on the projection-based solution. $\mathcal{R}_t$ denotes the retraction operator that ensures the updated result satisfies constant modulus, which lets $b_r^{(t+1)} = \frac{b_r^{(t)} + \epsilon_r^{(t)} \eta_r^{(t)}}{|b^{(t)} + \epsilon_r^{(t)} \eta_r^{(t)}|}$. $\boldsymbol{\epsilon}^{(t)}$ and $\boldsymbol{\eta}^{(t)}$ are the Armijo step size [40] and the search direction at the point $\mathbf{b}^{(t)}$, respectively. The search direction $\boldsymbol{\eta}^{(t)}$ lies in the tangent space of the complex circle manifold at the point $\mathbf{b}^{(t)}$, which is given by

$$
\boldsymbol{\eta}^{(t)} = -\operatorname{grad} g(\mathbf{b})
$$
$$
+ \zeta^{(t)}\left(\boldsymbol{\eta}^{(t-1)} - \operatorname{Re}\left(\boldsymbol{\eta}^{(t-1)} \circ \mathbf{b}^{(t)\dagger}\right) \circ \mathbf{b}^{(t)}\right), \tag{38}
$$

where notation $\dagger$ and $\circ$ conjugation denote the conjugation and Hadamard production, respectively, $\zeta^{(t)}$ is chosen as the Polak-Ribiere parameter [40], $\operatorname{grad} g(\mathbf{b})$ is the Riemannian gradient of $g(\mathbf{b})$, which calculated as the orthogonally projecting of the Euclidean gradient of $g(\mathbf{b})$, given by

$$
\operatorname{grad} g(\mathbf{b}) = \nabla g(\mathbf{b}) - \operatorname{Re}\left(\nabla g(\mathbf{b}) \circ \mathbf{b}^{(t)\dagger}\right) \circ \mathbf{b}^{(t)}, \tag{39}
$$

where $\nabla g(\mathbf{b})$ is the Euclidean gradient of $g(\mathbf{b})$, which defined as

$$
\nabla g(\mathbf{b}) = \frac{1}{2}\left(\overline{\mathbf{W}}^{H} \overline{\mathbf{W}} \mathbf{b} + e^{j2\pi} \overline{\mathbf{W}}^{H} \overline{\mathbf{W}} \mathbf{1}_N\right). \tag{40}
$$

C. Alternating Localization and DMA Tuning

The DMA tuning detailed above requires knowledge of the user position, whose estimation is the core of the localization problem. However, alternating optimization can extend it for joint DMA tuning and localization. The rationale here stems from the fact that the design of $\mathbf{Q}$ for COA-based localization realizes a form of beamforming, which in the radiating near-field specializes in beamfocusing [5]. Consequently, (25) can be regarded as designing $\mathbf{Q}$ to focus the received beam towards a given location and iteratively refine the specific localization.

Therefore, for the MLE process in (23), even when the focusing position at the array receiving end deviates from the actual

---

Algorithm 2: Iterative Optimization Algorithm for Alternating Localization and DMA Tuning.

Initialize: Initialize the matrix $\mathbf{Q}^1 \in \mathbb{C}^{N_\mathrm{d} \times N}$ constrained by the array architecture; $k = 1$; Iterations limit K.
  1: Obtain the position estimation $\mathbf{p}_\mathcal{M}$ by Algorithm 1 (Steps 1-4).
While $k \leq K$ **do**
  For $m = 1 : M$
  2: Estimate $\mathbf{p}_m^k$ by maximizing $f(\mathbf{p}_\mathcal{M}, \mathbf{Q}^k)$ (equivalently maximize the projection MLE defined in (22)).
  3: Update position set: $\mathbf{p}_\mathcal{M} = \mathbf{p}_{\mathcal{M}-m} \cup \mathbf{p}_m^k$.
  End
  4: Get $\mathbf{Q}^{k+1}$ by maximizing $f(\mathbf{p}_\mathcal{M}, \mathbf{Q})$ through solving (25).
  5: Update receive vector $\mathbf{y}^{k+1}$ from $\mathbf{Q}^{k+1}$ by (12).
  6: $k = k + 1$
End while
Output: The position estimation $\mathbf{p}_\mathcal{M}$.

---

source position, the estimated results are still improved,[2] which means that once we obtain a rough estimation of the source location, we can constantly approach the desired actual source position by updating the focus position. Meanwhile, the update of $\mathbf{Q}$ can be synchronized with the iteration in the AP algorithm, i.e., we can obtain a new alternating algorithm by embedding the update of $\mathbf{Q}$ into Algorithm 1.

The resulting alternating localization and DMA tuning algorithm is summarized as Algorithm 2. In Algorithm 2, we utilize the receiving vector from random coefficient response performing the initial position estimation and obtain new observations after updating the coefficients of $\mathbf{Q}$ with the results of the previous position estimation. We can repeat the above steps at each receiving time slot so that the estimated result is close to the actual source location gradually. An analogous alternating optimization strategy was employed in [50], where the author obtains the user's angle estimate using AOA method and subsequently employs it to formulate analog coefficients for distance estimation, known as the two-step method. However, unlike the algorithm we have put forth, the two-step method does not leverage distance information. Consequently, the analog coefficients design it yields is fundamentally grounded on a far-field model, leading to performance degradation when applied in near-field scenarios.

D. Extension to Fully Digital and Hybrid Architectures

In this part, we extend the proposed localization and tuning scheme to other antenna architectures.

1) Fully Digital Antenna: For the fully digital array, each antenna element is connected to a dedicated RF chain (without analog combining operation), leading to the received signal

---

[2]As we analysed, the improvement which yield from DMA tuning is caused by the focusing operation. Even if there is a mismatch between the focusing position and the actual user position, the focusing gain still exists while is only loss [42].

$\mathbf{y} = \mathbf{x}$. In this case, the likelihood function in (17) of $\mathbf{x}$, can be expressed as [18]:

$$\log p(\mathbf{x}; \mathbf{p}_\mathcal{M}) \propto \sum_{t=1}^{N_T} \|\mathcal{P}[\mathbf{S}_\mathrm{a}(\mathbf{p}_\mathcal{M})]\mathbf{x}(t)\|^2, \quad (41)$$

Since without analog domain design, by making $\mathbf{Q} = \mathbf{I}_N$ and $\mathbf{H} = \mathbf{I}_N$, we can directly use Algorithm 1 to implement localization.

2) Hybrid Phase-Shifter Antenna: When we consider the hybrid arrays, as previously introduced, the optimization of the phase shifters is similar to DMA tuning. Thus, Algorithm 1 also applies to the hybrid array case and just needs to let $\mathbf{H} = \mathbf{I}_N$. Besides, by replacing the constraints of matrix $\mathbf{Q}$ to (2) and (11), (25) can be regarded as optimizing the phase of the hybrid array to improve the MLE, which can be written as

$$\max_{\mathbf{Q}} \mathrm{tr}\left[\mathbf{Q}\mathbf{G}\mathbf{G}^H\mathbf{Q}^H\right]$$

$$\text{s.t. } \mathbf{Q}_{n,(i-1)N_\mathrm{e}+l} = \begin{cases} q_{i,l} \in \mathcal{F} & i = n. \\ 0 & i \neq n. \end{cases} \quad (42)$$

Problem (42) is almost identical to (27), except for the omission of the matrix $\mathbf{H}$. Thus it can obtain the solution from Theorem 1 directly by removing the effect of $\mathbf{H}$. The resulting phase is $\hat{q}_{i,l} = e^{j\psi_{i,l}^*}$, with $\psi_{i,l}^* = \frac{\sum_{m=1}^M v_{m,i,l}}{M}$.

Since without the requirement of projection of the phase solution onto Lorentzian constraint, the solution of (42) can be regarded as the optimal solution of the hybrid array. In fact, the Lorentzian constraint only has a negative effect on phase design. Therefore, hybrid arrays always outperform DMA under the same number of antennas and array aperture.

IV. NUMERICAL EVALUATIONS

This section evaluates the localization performance under multiple array architectures for different SNR scenarios. We first detail the simulation setup in Section IV-A, and present our numerical results in Section IV-B

A. Simulation Parameters

In our simulation study, we set the carrier frequency of the pilot signal as $f_\mathrm{p} = 28$ GHz, corresponding to a signal wavelength of $\lambda = 0.01$ m. In one observed time window, the sample number is set as $N_T = 500$. Then, we consider a localization scenario that the user is in the XY-plane, while the antennas of the array are lying on the YZ-plane, with the reference point of the array set at the origin of the coordinate system. In this case, the position of each user is expressed as $(\mathrm{x}_m, \mathrm{y}_m, 0)$ in Euclidean coordinate, or $(d_m, \theta_m, \pi/2)$ in polar coordinates. We simulate DMAs as well as hybrid phase-shifter antennas and fully digital ones. For DMAs, we set use $\alpha = 0.6\,\mathrm{m}^{-1}$ and $\beta = 827.67\,\mathrm{m}^{-1}$ to represent the propagation inside the DMA waveguides. The DMA array is comprised of N_d microstrips, i.e., it only requires N_d RF chains, with each microstrip containing N_e antenna elements. The total number of antenna elements is thus $N = N_\mathrm{d}N_\mathrm{e}$. The noise variance σ^2 is set to adjust the signal-to-noise ratio (SNR) as $\mathrm{SNR} = 10\log(\|\mathbf{x}\|^2/(N\sigma^2))$.

TABLE I
ARRAY ARCHITECTURE

Architecture	Antenna number	RF number
Full digital $\lambda/2$	N_1	N_1
DMA $\lambda/2$	N_1	N_{d}
Hybrid $\lambda/2$	N_1	N_{d}
DMA $\lambda/4$	N_2	N_{d}

The separation between microstrips is set as $5\lambda/2$, (the separation between rows of hybrid or fully digital arrays is also set in this way). In general, the antenna elements within the microstrip of DMAs are arranged at sub-wavelength spacing, while the antennas of full digital arrays and hybrid arrays require at least half-wavelength spacing to be arranged. To compare the performance differences of three antenna architectures in detail, we set two kinds of DMA microstrip antenna space, one set to $\lambda/2$ antenna spacing (as in the full digital case and hybrid case), and the other set to $\lambda/4$ antenna spacing (as in the general DMA case), the full digital array and hybrid array have the same dimensions as the DMA at the $\lambda/2$ spacing case. The number of antennas and required RF chains for each array are summarized in Table I. To make a fair comparison, we consider that the three antenna architectures have the same physical aperture equal to $D = \sqrt{2}L$, with L denoting the length of the microstrip. We fix $L = 25$ cm, thereby the number of microstrips in this DMA is $N_{\mathrm{d}} = 2L/(5\lambda) = 10$. For $\lambda/2$ spacing (antennas in each row of the full digital array is the same), the number of antenna elements of each microstrip is calculated as $N_{\mathrm{e}} = 2L/\lambda = 50$ and the total number of antenna elements is thus $N_1 = N_{\mathrm{d}}N_{\mathrm{e}} = 500$; For $\lambda/4$ spacing, $N_{\mathrm{e}} = 4L/\lambda = 100$ and thus $N_2 = 1000$. The above simulation setup is exploited throughout our simulations unless otherwise specified.

B. Numerical Results

The COA-based localization method is only applicable in the near field range, thus the source position $(d_m, \theta_m, \pi/2)$ should be located in the Fresnel region of the array, i.e., d_m should satisfy that

$$d_0 \leq d_{\mathrm{F}} = \frac{2D^2}{\lambda}, \tag{43}$$

where d_{F} is the Fraunhofer distance limit, which, under the current setting, equals $d_{\mathrm{F}} = 24$ meters. That is, the near-field region extends up to 24 meters.

To demonstrate this point, we provide a root mean square error (RMSE) heatmap to clarify the range of the proposed COA-based localization effectiveness, as shown in Fig. 5. We use the DMA as the example to localize one user (the relevant conclusions arising from this are also applicable to other antenna architectures), the DMA is $\lambda/2$ spacing. We consider a $50 \times 50 \, \mathrm{m}^2$ grid of points with a resolution of 1 m. Then, we set each grid point as the target user location to estimate the user position using Algorithm 2 with optimal DMA tuning design.
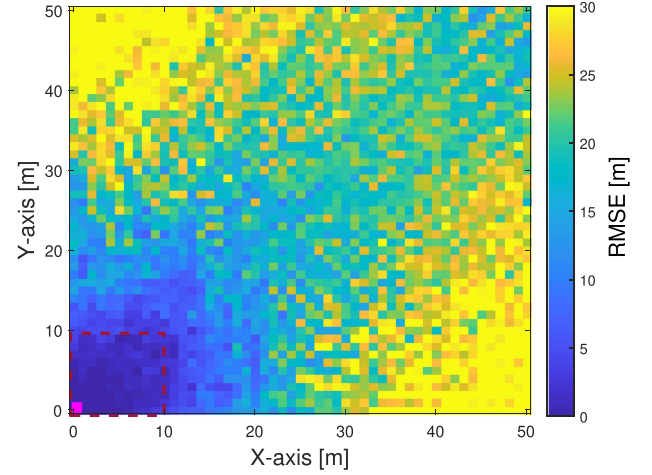

Fig. 5. The heatmap for position estimate RMSE under different user positions, with $N_{\mathrm{d}} = 10$ and $d_{\mathrm{F}} = 24$ meters, SNR is fixed as -10 dB. The magenta square denotes the array position.
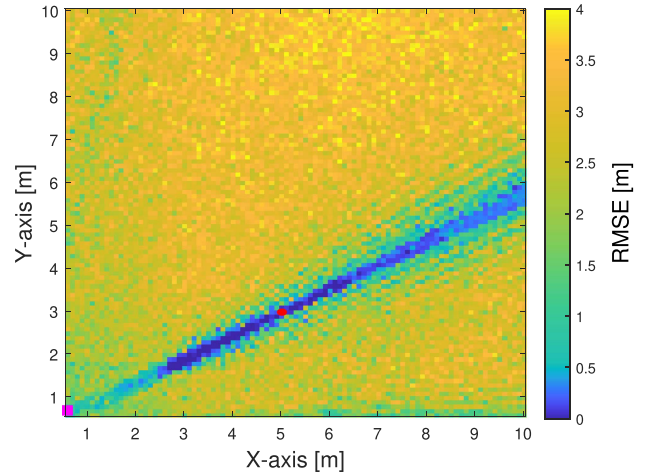

Fig. 6. The heatmap for the RMSE on user position estimate by varying user positions, SNR is fixed as -10 dB. The magenta square denotes the array position. The red point is the hypothetical position that $\mathbf{Q}$ focuses on, located at $d = 0.25\, d_{\mathrm{F}}$ meters, $\theta = \pi/6$.

The RMSE of each estimation is calculated as

$$\mathrm{RMSE} = \sqrt{\frac{1}{N_{\mathrm{mc}}} \sum_{n=1}^{N_{\mathrm{mc}}} e_n^2}, \tag{44}$$

where N_{mc} is the number of Monte Carlo iterations, $e_n^2 = |(\mathrm{x}, \mathrm{y}) - (\hat{\mathrm{x}}^{(n)}, \hat{\mathrm{y}}^{(n)})|^2$ is the squared localization error (i.e., the distortion), (x, y) is the source coordinates, and $(\hat{\mathrm{x}}^{(n)}, \hat{\mathrm{y}}^{(n)})$ are the estimated coordinates at the n-th Monte Carlo simulation. For the considered scenario, following the results reported in Fig. 5, the RMSE of estimations would be significantly reduced within the near field range.

To present in detail that our design of $\mathbf{Q}$ realizes a form of beam focusing, a heatmap is provided in Fig. 6. We consider a $10 \times 10 \, \mathrm{m}^2$ grid of points with the resolution of 0.1 meters, with the array located on the origin. Then, we set the user to transmit the pilot signal on each grid point, and the $\mathbf{Q}$ is
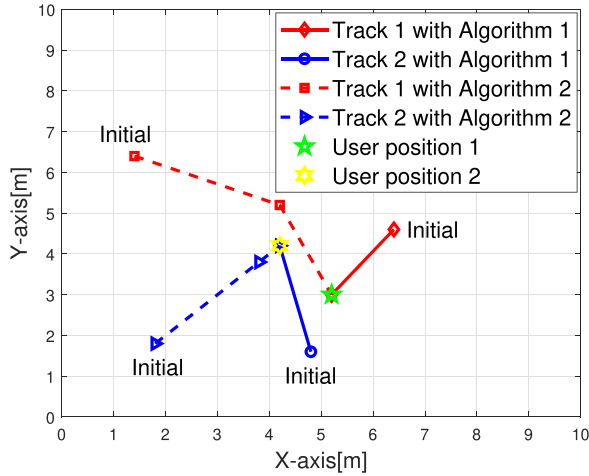
Fig. 7. Position estimations track map for each iteration of Algorithms 1 and 2, SNR is fixed as -5 dB, with user position: $d_1 = 0.25\,d_{\rm F}$ meters, $\theta_1 = \pi/6$; $d_2 = 0.25\,d_{\rm F}$ meters, $\theta_2 = \pi/4$.

Fig. 8. Contrast of the number of iterations required for convergence via multiple contrast schemes. $N_{\rm d} = 10$, $N_{\rm e} = 50$, SNR is fixed as -5 dB, user position is set as $d_1 = 0.25\,d_{\rm F}$ meters, $\theta_1 = \pi/6$, $d_2 = 0.25\,d_{\rm F}$ meters, $\theta_2 = \pi/4$.

designed to focus on the fixed point as shown (i.e., the $\mathbf{Q}$ is obtained by assuming the user is located on the setting fixed point and transmit the pilot signal). The DMA would localize the user based on the actual received pilot signal with the fixed $\mathbf{Q}$. In contrast to Fig. 5, it is evident that the RMSE depicted in Fig. 6 experiences notable enhancements solely when the user's position is situated proximate to the focus point of $\mathbf{Q}$. Conversely, in the lower left corner of Fig. 5, marked by the brown box, its RMSE values keeps low compared to those in Fig. 6. This is because, in Fig. 5, $\mathbf{Q}$ is always designed to focus on the actual user position, whereas in Fig. 6, the $\mathbf{Q}$ design follows a fixed focused point strategy. Then, we further demonstrate the effectiveness of the proposed localization algorithm, as shown in Fig. 7. In Algorithm 1, the localization is performed with a given $\mathbf{Q}$ by the proposed RCG solution. Even if it is not realistic because the actual user position is unknown, we assume that the given $\mathbf{Q}$ has been designed perfectly to achieve a fair comparison with Algorithm 2). Comparatively, in Algorithm 2, the localization and the $\mathbf{Q}$ design are carried out alternately. It can be seen that both tracks of the position estimate with two algorithms gradually approach the real user position from the initial position estimate with iteration. Besides, it should be noted that Algorithm 1 yields a more accurate initial position estimation compared to Algorithm 2, and the estimation iterates faster to the actual user position, which indicates the impact of the $\mathbf{Q}$ design on localization.

To investigate the effectiveness of the $\mathbf{Q}$ design of the joint localization and DMA tuning algorithm in more detail, we investigate the number of iterations for the convergence of the Algorithm 2, as shown in Fig. 8, wherein the RMSE is the average of that of two users. To illustrate the convergence process in detail, we compare the convergence process between the random scheme and the RCG schemes. Furthermore, for a comparative analysis with similar approaches, we also consider the far-field-based method outlined in [50]. The "DMA RCG" denotes localization by Algorithm 2, that obtaining the DMA tuning via the RCG-based method without prior knowledge
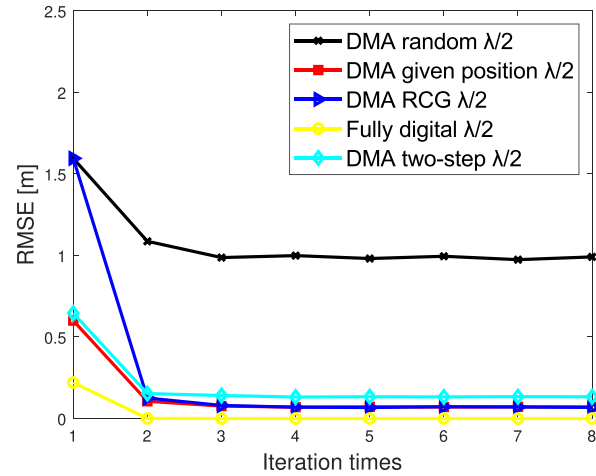
of user position, the "DMA given position" denotes directly localization by Algorithm 1, using the RCG-based method to get the DMA tuning which obtained from (32) ignoring the the issue of unknown users location. "DMA two-step" denotes localization using the two-step method where the DMA tuning is designed in a far field model. Specifically, this method entails the initial estimation of users' angle information in a far field model, as elaborated in [50]. Subsequently, $\mathbf{Q}$ is configured to align towards the direction of the users, facilitating near field localization by Algorithm 1 with this optimized $\mathbf{Q}$.

In Fig. 8, it can be seen that the RMSE of the DMA RCG scheme converges from the random scheme to the same RMSE as the DMA given position scheme. The DMA two-step scheme, as previously discussed, because DMA tuning is devised using a far-field model, it can only achieve directional alignment. Consequently, its efficacy in enhancing positioning performance is sub-optimal compared to our proposed DMA RCG scheme, a distinction that can be observed in Fig. 8. In addition, the speed of convergence depends on the accuracy of the initial position estimation, and the accuracy of the initial position estimation is related to the performance of the localization scheme thus the fully digital array always converges the fastest, while the DMA optimal scheme could achieve a close converge speed to the fully digital. The alternating scheme generally requires more convergence times than the DMA opt-prior scheme, not only due to the initial position estimation but also because of its additional update for matrix $\mathbf{Q}$. Therefore, the DMA opt scheme compromises the DMA opt-prior scheme and the random scheme. However, it can be seen that the iteration of matrix $\mathbf{Q}$ is also efficient; only one additional iteration at most is required to converge to the optimal.

We show the effectiveness of the analog domain design scheme we proposed in Fig. 9 which reports the RMSE of location estimation via different schemes under different SNRs. We considered a two-user localization scenario, where the caption describes the user's location. The curve "DMA RCG" and "DMA projection" denote the DMA tuning scheme for
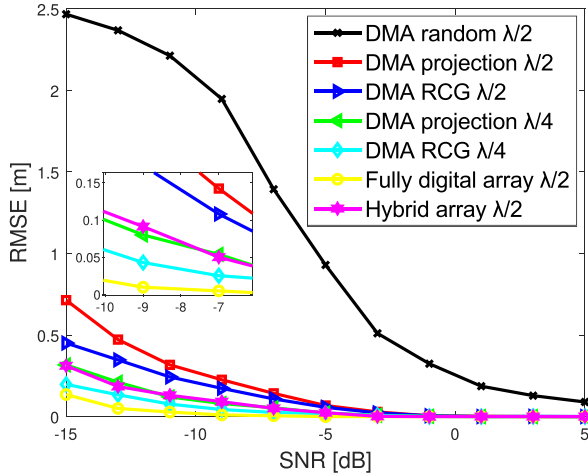
Fig. 9. Distortion contrast of multiple contrast schemes under different SNR with user position: $d_1 = 0.25\,d_F$ meters, $\theta_1 = \pi/6$; $d_2 = 0.25\,d_F$ meters, $\theta_2 = \pi/4$. $N_d = 10$, N_e is determined with the antenna space, $N_e = 50$ in $\lambda/2$ case, $N_e = 100$ in $\lambda/4$ case.

Fig. 10. Distortion contrast of multiple contrast schemes under different RF chain numbers. SNR $= -15$ dB, with user position: $d_1 = 0.25\,d_F$ meters, $\theta_1 = \pi/6$; $d_2 = 0.25$ meters, $\theta_2 = \pi/4$.

localization using Algorithm 2 with optimization $\mathbf{Q}$ from projection-based solution and RCG-based solution, respectively. To indicate the performance improvement from tuning design, the DMA random scheme and the fully digital scheme are also provided for comparison, where the DMA random scheme is obtained by setting a set of random coefficients for $\mathbf{Q}$, while the fully digital scheme localizes the user with MLE method [25] based on the fully digital array we just set. As shown in Fig. 9, the DMA random scheme yields higher RMSE than fully digital schemes, especially in the low SNR case. This is because the tunable coefficients matrix in the DMA random scheme represents only an interference effect for the MLE process. By tuning the DMA using Algorithm 2, one significantly improves the RMSE, and the RCG-based scheme achieved better performance compared to the projection-based scheme; thus, in the next experiments, we use the RCG-base scheme as the representative of the DMA tuning scheme. Without the Lorentzian constraint interference, the hybrid array scheme always outperforms DMA at the same number of antennas. Meanwhile, the DMA tuning scheme with $\lambda/4$ spacing would further reduce RMSE by increasing the number of microstrip elements compared to the DMA tuning scheme with $\lambda/2$ spacing using the same tuning scheme.

However, as shown in Fig. 9, the RMSE of the DMA tuning scheme or hybrid array scheme with $\lambda/2$ antenna spacing is still higher than the fully digital schemes due to the reduction of signal dimension, even the DMA tuning scheme with $\lambda/4$ can only reduce this performance loss. This is because the reduction of the RF chain can be seen as compression to the original received signal, resulting in inherent information loss. This also means that the increase in output signal dimension will alleviate the performance loss caused by compression behavior. In Fig. 10, we discussed the impact of the number of RF chains on localization performance under the same DMA optimization. All arrays maintain the same aperture, while the arrangement density of microstrips controls the number of RF chains. As a comparison,
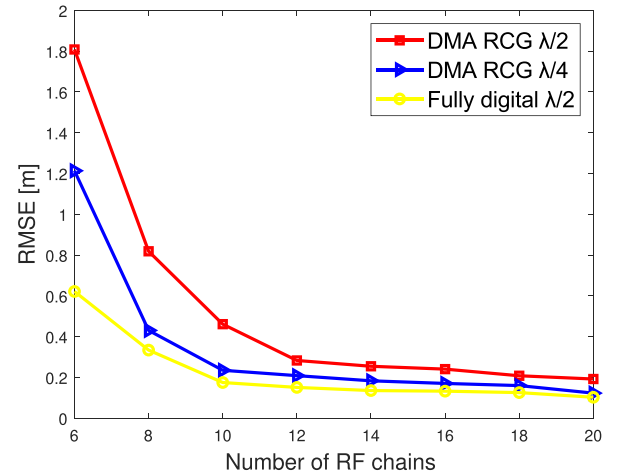
the fully digital array is also provided, and in the same aperture, the RF chain number of the fully digital array is 50 times that of the DMA. With the increase in the number of RF chains, the performance of all schemes has improved as the antenna number increased. Among them, the DMA tuning scheme made more significant progress than the fully digital scheme, where the DMA scheme with $\lambda/4$ achieved a performance similar to that of the full-digital array scheme. This demonstrates our point and indicates that for DMA, the increased number of elements combined with their proper tuning via Algorithm 2 can achieve similar localization accuracy compared with fully digital arrays utilizing $\times 50$ more RF chains.

V. CONCLUSION

In this work, we studied near-field multi-source position estimation based on the RF chain reduction array. Initially, we introduced comprehensive models tailored for radiating near-field position estimation systems across various antenna architectures. Subsequently, we formulated the optimization of the adjustable analog coefficients to enhance the accuracy of position estimates. By deriving the optimal analog coefficient design based on a known user position, we illustrated that the optimal analog coefficients for the aforementioned array in the near field effectively achieve beam focusing on the user's position. Building on this insight, we put forth an efficient algorithm for the joint estimation of position and the design of adjustable coefficients, eliminating the necessity for prior knowledge of the user's position. Numerical results show that the proposed design of adjustable coefficients of RF chain reduction array could significantly improve the near-field multi-source localization performance, reaching a fully digital implementation with at least one order of RF chain reduction. Meanwhile, to improve near-field localization accuracy, our proposed alternating localization and beam-focusing algorithm induces a beam-focusing effect.

APPENDIX A

Proof of Theorem 1: Rewrite (27) in scalar form:

$$\max_{q_{i,l}} \sum_{i=1}^{N_d} \sum_{m=1}^{M} \left| \sum_{l=1}^{N_e} q_{i,l} h_{i,l} g_{m,i,l} \right|^2, \quad \text{s.t. } q_{i,l} \in \mathcal{F}. \quad (A.1)$$

Equation (A.1) can be decomposed into N_d sub-problems, where each sub-problem represents the optimization on the corresponding DMA microstrip. Substituting the expression of $g_{m,i,l}$ in (6) into (A.1), and letting $q_{i,l} = e^{j\psi_{i,l}}$, we have the i-th sub-problem:

$$\max_{\psi_{i,l}} \sum_{m=1}^{M} \left| \sum_{l=1}^{N_e} a_{m,i,l} e^{-\rho_{i,l}\alpha_i} e^{-jv_{m,i,l}} e^{-j\rho_{i,l}\beta_i} e^{j\psi_{i,l}} \right|^2. \quad (A.2)$$

The optimal solution of (A.1) can be obtained by solving sub-problem (A.2) separately. It can be observed that the objective function of (A.2) is composed by M quadratic terms, where m-th term represents the phase adjustment of i-th microstrip on the received signal from m-th user, i.e., (A.2) can be regarded as finding the global optimal phase design for all users. To this purpose, we firstly calculate the local optimal solution for the m-th user. Specifically, to maximize the m-th term of (A.2), according to the triangle inequality, we have

$$\psi_{i,l}^{*(m)} = v_{m,i,l} + \rho_{i,l}\beta_i. \quad (A.3)$$

The global optimal solution for (A.2) should achieve a trade-off between all $\{\psi_{i,l}^{*(m)}\}_{m=1}^{M}$, i.e., it should achieves the minimum sum of Euclidean distances for all local optimal solutions, which can be calculated as

$$\min_{\psi_{i,l}} \mathrm{C}(\psi_{i,l}) = \sum_{m=1}^{M} \left| \psi_{i,l} - \psi_{i,l}^{*(m)} \right|^2. \quad (A.4)$$

Obviously (A.4) is convex, and the (optimal) solution can be found by solving the following equation

$$\frac{\partial \left(\mathrm{C}(\psi_{i,l}) \right)}{\partial \left(\psi_{i,l} \right)} = 2M\psi_{i,l} - 2\sum_{m=1}^{M} \psi_{i,l}^{*(m)} = 0. \quad (A.5)$$

whose solution is given by

$$\psi_{i,l}^{*} = \frac{\sum_{m=1}^{M} v_{m,i,l}}{M} + \rho_{i,l}\beta_i. \quad (A.6)$$

This proves the theorem. □

REFERENCES

[1] C. De Lima et al., "Convergent communication, sensing and localization in 6G systems: An overview of technologies, opportunities and challenges," *IEEE Access*, vol. 9, pp. 26902–26925, 2021.

[2] Z. Wang, Z. Liu, Y. Shen, A. Conti, and M. Z. Win, "Location awareness in beyond 5G networks via reconfigurable intelligent surfaces," *IEEE J. Sel. Areas Commun.*, vol. 40, no. 7, pp. 2011–2025, Jul. 2022.

[3] G. Torcolacci et al., "Holographic imaging with XL-MIMO and RIS: Illumination and reflection design," *IEEE J. Sel. Top. Signal Process.*, vol. 18, no. 4, pp. 587–602, May 2024.

[4] D. T. Bellini, D. Tagliaferri, M. Mizmizi, S. Tebaldini, and U. Spagnolini, "Multi-view near-field imaging in NLOS with non-reconfigurable EM skins," in *Proc. IEEE Int. Conf. Commun. Workshops*, Denver, CO, USA, 2024, pp. 384–389.

[5] P. Nepa and A. Buffi, "Near-field-focused microwave antennas: Near-field shaping and implementation," *IEEE Antennas Propag. Mag.*, vol. 59, no. 3, pp. 42–53, Jun. 2017.

[6] H. Zhang, N. Shlezinger, F. Guidi, D. Dardari, and Y. C. Eldar, "6G wireless communications: From far-field beam steering to near-field beam focusing," *IEEE Commun. Mag.*, vol. 61, no. 4, pp. 72–77, Apr. 2023.

[7] I. Ahmed et al., "A survey on hybrid beamforming techniques in 5G: Architecture and system model perspectives," *IEEE Commun. Surveys Tut.*, vol. 20, no. 4, pp. 3060–3097, Fourthquarter 2018.

[8] R. Méndez-Rial, C. Rusu, N. González-Prelcic, A. Alkhateeb, and R. W. Heath, "Hybrid MIMO architectures for millimeter wave communications: Phase shifters or switches?," *IEEE Access*, vol. 4, pp. 247–267, 2016.

[9] L. Taponecco, A. D'Amico, and U. Mengali, "Joint TOA and AOA estimation for UWB localization applications," *IEEE Trans. Wireless Commun.*, vol. 10, no. 7, pp. 2207–2217, Jul. 2011.

[10] D. Dardari, P. Closas, and P. M. Djurić, "Indoor tracking: Theory, methods, and technologies," *IEEE Trans. Veh. Technol.*, vol. 64, no. 4, pp. 1263–1278, Apr. 2015.

[11] H. Zhang, H. Zhang, B. Di, K. Bian, Z. Han, and L. Song, "Metalocalization: Reconfigurable intelligent surface aided multi-user wireless indoor localization," *IEEE Trans. Wireless Commun.*, vol. 20, no. 12, pp. 7743–7757, Dec. 2021.

[12] A. Guerra, F. Guidi, and D. Dardari, "Single-anchor localization and orientation performance limits using massive arrays: MIMO vs. beamforming," *IEEE Trans. Wireless Commun.*, vol. 17, no. 8, pp. 5241–5255, Aug. 2018.

[13] A. Elzanaty, A. Guerra, F. Guidi, D. Dardari, and M.-S. Alouini, "Towards 6G holographic localization: Enabling technologies and perspectives," *IEEE Internet Things Mag.*, vol. 6, no. 3, pp. 138–143, Sep. 2023.

[14] D. Dardari, N. Decarli, A. Guerra, and F. Guidi, "LOS/NLOS near-field localization with a large reconfigurable intelligent surface," *IEEE Trans. Wireless Commun.*, vol. 21, no. 6, pp. 4282–4294, Jun. 2022.

[15] M. Z. Win, Z. Wang, Z. Liu, Y. Shen, and A. Conti, "Location awareness via intelligent surfaces: A path toward holographic NLN," *IEEE Veh. Technol. Mag.*, vol. 17, no. 2, pp. 37–45, Jun. 2022.

[16] N. González-Prelcic et al., "The integrated sensing and communication revolution for 6G: Vision, techniques, and applications," *Proc. IEEE*, vol. 112, no. 7, pp. 676–723, Jul. 2024.

[17] F. Guidi and D. Dardari, "Radio positioning with EM processing of the spherical wavefront," *IEEE Trans. Wireless Commun.*, vol. 20, no. 6, pp. 3571–3586, Jun. 2021.

[18] Y.-D. Huang and M. Barkat, "Near-field multiple source localization by passive sensor array," *IEEE Trans. Antennas Propag.*, vol. 39, no. 7, pp. 968–975, Jul. 1991.

[19] B. Ferguson and R. Wyber, "Wavefront curvature passive ranging in a temporally varying sound propagation medium," in *Proc. MTS/IEEE Oceans, Ocean Odyssey*, vol. 4, 2001, pp. 2359–2365.

[20] L. Khamidullina, I. Podkurkov, and M. Haardt, "Conditional and unconditional Cramér-Rao bounds for near-field localization in bistatic MIMO radar systems," *IEEE Trans. Signal Process.*, vol. 69, pp. 3220–3234, 2021.

[21] A. A. D'Amico, A. d. J. Torres, L. Sanguinetti, and M. Win, "Cramér-Rao bounds for holographic positioning," *IEEE Trans. Signal Process.*, vol. 70, pp. 5518–5532, 2022.

[22] A. Elzanaty, A. Guerra, F. Guidi, and M.-S. Alouini, "Reconfigurable intelligent surfaces for localization: Position and orientation error bounds," *IEEE Trans. Signal Process.*, vol. 69, pp. 5386–5402, 2021.

[23] X. Zhang and H. Zhang, "Hybrid reconfigurable intelligent surfaces-assisted near-field localization," *IEEE Commun. Lett.*, vol. 27, no. 1, pp. 135–139, Jan. 2023.

[24] X. Gan, C. Huang, Z. Yang, C. Zhong, and Z. Zhang, "Near-field localization for holographic RIS assisted mmWave systems," *IEEE Commun. Lett.*, vol. 27, no. 1, pp. 140–144, Jan. 2023.

[25] A. Guerra, F. Guidi, D. Dardari, and P. M. Djurić, "Near-field tracking with large antenna arrays: Fundamental limits and practical algorithms," *IEEE Trans. Signal Process.*, vol. 69, pp. 5723–5738, 2021.

[26] X. Zhang, W. Chen, W. Zheng, Z. Xia, and Y. Wang, "Localization of near-field sources: A reduced-dimension MUSIC algorithm," *IEEE Commun. Lett.*, vol. 22, no. 7, pp. 1422–1425, Jul. 2018.

[27] C. Cheng, S. Liu, H. Wu, and Y. Zhang, "An efficient maximum-likelihood-like algorithm for near-field coherent source localization," *IEEE Trans. Antennas Propag.*, vol. 70, no. 7, pp. 6111–6116, Jul. 2022.

[28] M. Rahal et al., "Performance of RIS-aided near-field localization under beams approximation from real hardware characterization," *EURASIP J. Wireless Commun. Netw.*, vol. 2023, no. 1, 2023, Art. no. 86.

[29] S. Yue, S. Zeng, L. Liu, Y. C. Eldar, and B. Di, "Hybrid near-far field channel estimation for holographic MIMO communications," *IEEE Trans. Wireless Commun.*, vol. 23, no. 11, pp. 15798–15813, Nov. 2024.

[30] K. Hu, S. P. Chepuri, and G. Leus, "Near-field source localization: Sparse recovery techniques and grid matching," in *Proc. IEEE 8th Sensor Array Multichannel Signal Process. Workshop*, 2014, pp. 369–372.

[31] Z. Li, J. Shen, H. Zhai, and X. Zhang, "3-D localization for near-field and strictly noncircular sources via centro-symmetric cross array," *IEEE Sensors J.*, vol. 21, no. 6, pp. 8432–8440, Mar. 2021.

[32] T. Zirtiloglu, N. Shlezinger, Y. C. Eldar, and R. Tugce Yazicigil, "Power-efficient hybrid MIMO reciever with task-specific beamforming using low-resolution ADCs," in *Proc. IEEE Int. Conf. Acoust., Speech, Signal Process.*, 2022, pp. 5338–5342.

[33] Y. Zeng and R. Zhang, "Millimeter wave MIMO with lens antenna array: A new path division multiplexing paradigm," *IEEE Trans. Commun.*, vol. 64, no. 4, pp. 1557–1571, Apr. 2016.

[34] Z. Abu-Shaban, K. Keykhosravi, M. F. Keskin, G. C. Alexandropoulos, G. Seco-Granados, and H. Wymeersch, "Near-field localization with a reconfigurable intelligent surface acting as lens," in *Proc. IEEE Int. Conf. Commun.*, 2021, pp. 1–6.

[35] O. Levy and N. Shlezinger, "Rapid hybrid modular receive beamforming via learned optimization," in *Proc. IEEE Int. Conf. Acoust., Speech, Signal Process.*, 2024, pp. 12826–12830.

[36] T. Gong, N. Shlezinger, S. S. Ioushua, M. Namer, Z. Yang, and Y. C. Eldar, "RF chain reduction for MIMO systems: A hardware prototype," *IEEE Syst. J.*, vol. 14, no. 4, pp. 5296–5307, Dec. 2020.

[37] O. Lavi and N. Shlezinger, "Learn to rapidly and robustly optimize hybrid precoding," *IEEE Trans. Commun.*, vol. 71, no. 10, pp. 5814–5830, Oct. 2023.

[38] N. Shlezinger, G. C. Alexandropoulos, M. F. Imani, Y. C. Eldar, and D. R. Smith, "Dynamic metasurface antennas for 6G extreme massive MIMO communications," *IEEE Wireless Commun.*, vol. 28, no. 2, pp. 106–113, Apr. 2021.

[39] N. Shlezinger, G. C. Alexandropoulos, M. F. Imani, Y. C. Eldar, and D. R. Smith, "Dynamic metasurface antennas for uplink massive MIMO systems," *IEEE Trans. Commun.*, vol. 67, no. 10, pp. 6829–6843, Oct. 2019.

[40] H. Zhang, N. Shlezinger, F. Guidi, D. Dardari, M. F. Imani, and Y. C. Eldar, "Beam focusing for near-field multi-user MIMO communications," *IEEE Trans. Wireless Commun.*, vol. 21, no. 9, pp. 7476–7490, Sep. 2022.

[41] Q. Yang et al., "Near-field localization with dynamic metasurface antennas," in *Proc. IEEE Int. Conf. Acoust., Speech, Signal Process.*, 2023, pp. 1–5.

[42] P. Gavriilidis and G. C. Alexandropoulos, "Near-field beam tracking with extremely large dynamic metasurface antennas," 2024, *arXiv:2406.01488*.

[43] J. S. Herd and M. D. Conway, "The evolution to modern phased array architectures," *Proc. IEEE*, vol. 104, no. 3, pp. 519–529, Mar. 2016.

[44] S. S. Ioushua and Y. C. Eldar, "A family of hybrid analog–digital beamforming methods for massive MIMO systems," *IEEE Trans. Signal Process.*, vol. 67, no. 12, pp. 3243–3257, Jun. 2019.

[45] T. Sleasman et al., "Waveguide-fed tunable metamaterial element for dynamic apertures," *IEEE Antennas Wireless Propag. Lett.*, vol. 15, pp. 606–609, 2016.

[46] C. L. Holloway, E. F. Kuester, J. A. Gordon, J. O'Hara, J. Booth, and D. R. Smith, "An overview of the theory and applications of metasurfaces: The two-dimensional equivalents of metamaterials," *IEEE Antennas Propag. Mag.*, vol. 54, no. 2, pp. 10–35, Apr. 2012.

[47] L. Huang, T. Long, E. Mao, and H. C. So, "MMSE-Based MDL method for robust estimation of number of sources without eigendecomposition," *IEEE Trans. Signal Process.*, vol. 57, no. 10, pp. 4135–4142, Oct. 2009.

[48] I. Ziskind and M. Wax, "Maximum likelihood localization of multiple sources by alternating projection," *IEEE Trans. Acoust., Speech, Signal Process.*, vol. 36, no. 10, pp. 1553–1560, Oct. 1988.

[49] H. Zhang, N. Shlezinger, F. Guidi, D. Dardari, M. F. Imani, and Y. C. Eldar, "Near-field wireless power transfer with dynamic metasurface antennas," in *Proc. IEEE Int. Workshop Signal Process. Adv. Wireless Commun.*, 2022, pp. 1–5.

[50] S. K. Dehkordi et al., "Multistatic parameter estimation in the near/far field for integrated sensing and communication," *IEEE Trans. Wireless Commun.*, vol. 23, no. 12, pp. 17929–17944, Dec. 2024.

Qianyu Yang (Graduate Student Member, IEEE) received the B.S. degree from Northeast University, Shenyang, China, in 2019. He is currently working toward the Ph.D degree with the School of Communications and Information Engineering, Nanjing University of Posts and Telecommunications, Nanjing, China. His research interests include 6G near-field MIMO technologies, near-field localization, and wireless power transfer.

Anna Guerra (Member, IEEE) received the B.Sc., M.Sc., and Ph.D. degrees in Electronics, Telecommunications, and Information Technologies from the University of Bologna (UNIBO), Bologna, Italy, in 2009, 2012, and 2016, respectively. From 2016 to 2021, she was a Postdoctoral Researcher with UNIBO. From 2021 to 2024, she was a Researcher with the National Research Council of Italy. She is currently an Associate Professor with the Department of Electrical, Electronic and Information Engineering, UNIBO. During 2018–2020, she was awarded a global Marie Skłodowska-Curie research fellowship for the H2020 AirSens project, spending the project's outgoing phase with Stony Brook University, Stony Brook, NY, USA. In 2023, she received an ERC Starting Grant fellowship for the CUE-GO project. She was the recipient of several awards, including the Best Student Paper Award at the 2014 IEEE International Conference on Ultra-Wideband (Paris, France), the Best Paper Award at the 2019 IEEE RFID-TA Conference Pisa, Italy, and the Best Paper Award at the 2021 IEEE International Conference on Autonomous Systems Montreal, QC, Canada. She was an Associate Editor for IEEE TRANSACTIONS ON WIRELESS COMMUNICATIONS, IEEE COMMUNICATIONS LETTERS, and IEEE WIRELESS COMMUNICATIONS LETTERS.

Francesco Guidi (Member, IEEE) received the M.S. degree (summa cum laude) in electronics and telecommunications engineering from the University of Bologna, Bologna, Italy, in 2009, and the joint Ph.D. degree in information engineering from École Polytechnique, Paris, France, and the University of Bologna, in 2013. From 2015 to 2017, he held a research position funded by an individual European Marie-Curie Fellowship with the French Alternative Energies and Atomic Energy Commission (CEA), LETI, in Grenoble, France. He is currently a Senior Researcher with the National Research Council of Italy, the Institute of Electronics, Computer, and Telecommunication Engineering. He was recipient of the Best Student Paper Award at the International Conference on UltrawideBand Paris, France in 2014, and the Best Paper Award at the International Conference on Autonomous Systems Montreal, Canada in 2021. In 2022 and 2023, he was recognized as an Exemplary Reviewer for IEEE COMMUNICATIONS LETTERS. He is currently an Associate Editor for IEEE WIRELESS COMMUNICATIONS LETTERS and IEEE TRANSACTIONS ON COMMUNICATIONS, and as a Guest Editor for the IEEE INTERNET OF THINGS Journal and IEEE TRANSACTIONS ON AEROSPACE AND ELECTRONIC SYSTEMS.

Nir Shlezinger (Senior Member, IEEE) received the B.Sc., M.Sc., and Ph.D. degrees in electrical and computer engineering from Ben Gurion University, Beersheba, Israel, in 2011, 2013, and 2017, respectively. From 2017 to 2019, he was a Postdoctoral Researcher with the Technion, Haifa, Israel and from 2019 to 2020, he was a Postdoctoral Researcher with the Weizmann Institute of Science, Rehovot, Israel where he was awarded the FGS Prize for his research achievements. He is currently an Assistant Professor with the School of Electrical and Computer Engineering with BenGurion University. He was the recipient of the 2024 IEEE ComSoc Fred W. Ellersick Award, and the 2024 Krill Prize for outstanding young researchers. His research interests include communications, information theory, signal processing, and machine learning.

Haiyang Zhang (Member, IEEE) received the B.S. degree in communication engineering from Lanzhou Jiaotong University, Lanzhou, China, in 2009, the M.S. degree in information and communication engineering from the Nanjing University of Posts and Telecommunications, Nanjing, China, in 2012, and the Ph.D. degree in information and communication engineering from Southeast University, Nanjing, China, in 2017. From 2017 to 2020, he was a Postdoctoral Research Fellow with the Singapore University of Technology and Design, Singapore. From 2020 to 2022, he was a Postdoctoral Research Fellow with the Weizmann Institute of Science, Israel, where he was awarded the FGS Prize for outstanding research achievements. He is currently a Professor with the School of Communications and Information Engineering, Nanjing University of Posts and Telecommunications. His research interests include 6G near-field MIMO communications, deep learning, and sampling theory. He is/was the Co-Chair of the IEEE ICC Workshop on 6G Near-Field Communications. He is a Guest Editor for the IEEE INTERNET OF THINGS Journal and IEEE TRANSACTIONS ON AEROSPACE AND ELECTRONIC SYSTEMS.

Davide Dardari (Fellow, IEEE) is currently a Full Professor with the University of Bologna, Bologna, Italy. He has been a Research Affiliate with the Massachusetts Institute of Technology, Cambridge, MA, USA. He was the Chair of the Radio Communications Committee and a Distinguished Lecturer during 2018–2019 of the IEEE Communications Society. His research interests include in wireless communications, localization techniques, smart radio environments, and distributed signal processing. He was the recipient of the IEEE Aerospace and Electronic Systems Society's M. Barry Carlton Award 2011 and the IEEE Communications Society Fred W. Ellersick Prize 2012. He was the Editor of IEEE TRANSACTIONS ON WIRELESS COMMUNICATIONS from 2006 to 2012. He is currently a Senior Member of the Editorial Board of the IEEE Signal Processing Magazine.

Baoyun Wang (Member, IEEE) received the Ph.D. degree in electrical engineering from Southeast University, Nanjing, China, in 1997. From 1999 to 2000, he was a Postdoctoral Research Fellow with the Department of Computer Science and Engineering, Pohang University of Science and Technology, Pohang, South Korea. He is currently a Full Professor in electrical engineering with the Nanjing University of Posts and Telecommunications, Nanjing. His research interests include information theory, statistical signal processing, graph theory, and their applications in wireless communications.

Yonina C. Eldar (Fellow, IEEE) received the B.Sc. degree in physics and the B.Sc. degree in electrical engineering from Tel-Aviv University, Tel-Aviv, Israel, 1995 and 1996, respectively, and the Ph.D. degree in electrical engineering and computer science from the Massachusetts Institute of Technology (MIT), Cambridge, MA, USA, in 2002. She was a Professor with the Department of Electrical Engineering, Technion, where she held the Edwards Chair in Engineering. She is currently a Professor with the Department of Mathematics and Computer Science, Weizmann Institute of Science, Rehovot, Israel. She is also a Visiting Professor with MIT, a Visiting Scientist with the Broad Institute, and an Adjunct Professor with Duke University, and was a Visiting Professor with Stanford. She is also a highly cited Researcher. She is a member of the Israel Academy of Sciences and Humanities (elected 2017) and a EURASIP Fellow. She is also the author of the book *Sampling Theory: Beyond Bandlimited Systems* and coauthor of four other books published by Cambridge University Press. Her research interests include statistical signal processing, sampling theory and compressed sensing, learning and optimization methods, and their applications to biology, medical imaging and optics. Dr. Eldar was the recipient of many awards for excellence in research and teaching, including the IEEE Signal Processing Society Technical Achievement Award (2013), the IEEE/AESS Fred Nathanson Memorial Radar Award (2014), and IEEE Kiyo Tomiyasu Award (2016). She was a Horev Fellow of the Leaders in Science and Technology program with the Technion and an Alon Fellow. She was the recipient of the Michael Bruno Memorial Award from the Rothschild Foundation, Weizmann Prize for Exact Sciences, the Wolf Foundation Krill Prize for Excellence in Scientific Research, Henry Taub Prize for Excellence in Research (twice), Hershel Rich Innovation Award (three times), Award for Women with Distinguished Contributions, Andre and Bella Meyer Lectureship, Career Development Chair with the Technion, Murieland David Jacknow Award for Excellence in Teaching, and the Technions Award for Excellence in Teaching (two times). She was also the recipient of several best paper awards and best demo awards together with her research students and colleagues including the SIAM outstanding Paper Prize, UFFC Outstanding Paper Award, Signal Processing Society Best Paper Award and the IET Circuits, Devices and Systems Premium Award, and was selected as one of the 50 most influential women in Israel and in Asia. She was a member of the Young Israel Academy of Science and Humanities and the Israel Committee for Higher Education. She is the Editor-in-Chief for Foundations and Trends in Signal Processing, a member of the IEEE Sensor Array and Multichannel Technical Committee and serves on several other IEEE committees. Formerly, she was a Signal Processing Society Distinguished Lecturer, a member of the IEEE Signal Processing Theory and Methods and Bio Imaging Signal Processing technical committees, and was an Associate Editor for the IEEE TRANSACTIONS ON SIGNAL PROCESSING, EURASIP Journal of Signal Processing, SIAM Journal on Matrix Analysis and Applications, and SIAM Journal on Imaging Sciences. She was the Co-Chair and Technical Co-Chair of several international conferences and workshops.